

Research Article

Nonuniformly Spaced Array with the Direct Data Domain Method for 2D Angle-of-Arrival Measurement in Electronic Support Measures Application from 6 to 18 GHz

Chen Wu  and Janaka Elangage

Defence Research and Development Canada, Ottawa Research Centre, Ottawa K1A 0Z4, Canada

Correspondence should be addressed to Chen Wu; chen.wu@drdc-rddc.gc.ca

Received 27 May 2020; Revised 24 July 2020; Accepted 3 August 2020; Published 2 September 2020

Guest Editor: Jingjing Cai

Copyright © 2020 Chen Wu and Janaka Elangage. This is an open access article distributed under the Creative Commons Attribution License, which permits unrestricted use, distribution, and reproduction in any medium, provided the original work is properly cited.

This paper introduces a 2D angle-of-arrival (AoA) estimator, which has a 6–18 GHz 7-element nonuniformly spaced array (NSA) and a Direct Data Domain- (D3-) based AoA algorithm for a 2D isotropic-element planar array (IEPA). A 2D calibration and data-transformation method is developed to convert the NSA data to the output of the IEPA, so that the NSA-measured data can be used in the D3 algorithm. Using the steering vector (SV) of the IEPA and the results derived from the D3 method, a new 2D AoA searching method is also developed, which offers frequency-independent performance defined by the probability of AoA estimation, when the required estimation accuracy and signal-to-noise ratio (SNR) are given. For the applications of electronic support measures, this paper also presents the use of precalculated SV and data-transformation matrix databases built on preselected frequency points and a 2D-angle grid that is close to uniformly distributed directions. The simulation results show that with good SNR (≥ 15 dB), the estimator can have 50% probability of AoA estimation with root mean square error (RMSE) less than or equal to 1° using just a few samples from the NSA. Moreover, the study focuses on the applications with low SNR by using more samples from the NSA. Results show that the estimator has 52% and 80% probabilities of AoA estimation with $\text{RMSE} \leq 1^\circ$ and 5° , respectively, for phase- or frequency-modulated radar pulses, when the SNR is within $[-10, 0]$ dB. The study also shows that the estimator prefers a circular-shaped planar array with a triangular interelement pattern, since it presents more symmetrical characteristics from different azimuth angles.

1. Introduction

The angle-of-arrival (AoA) of the signal of interest (SOI) is the most important measurement parameter in an electronic support measures (ESM) system to de-interleave intercepted radar signals, especially in detecting and classifying low probability of intercept signals [1]. Traditionally, spinning direction-finding (DF) antenna, amplitude-comparison, phase-comparison, and interferometry methods are popular AoA measurement methods in ESM systems [2–10]. In addition, there are many microwave DF systems developed for wireless communication applications [11]. From a signal-processing perspective, there are a number of algorithms used for signal DF applications. Among them, multiple signal classification (MUSIC) [12] and estimation of signal

parameters via rotation invariance techniques (ESPIRT) [13] have been used for many years with different array configurations for different applications. As examples, currently, these methods are used for 2D AoA estimations for mixed circular and noncircular incident signals for massive multiple-input multiple-output systems [14] and for uniform rectangular array [15]. However, to apply these methods, a stable signal environment is generally required, since the signal covariance matrix needs to be formed. A new approach for AoA estimation was introduced using information geometry (IG) [16]. Based on IG, Dong et al. [17] introduced a simple scaling transform-based information geometry (STRIG) method, which has more consistent performance than the original IG method while having a high AoA estimation resolution. Lonkeng and Zhuang [18]

presented a research on 2D DF estimation using arbitrary arrays in MIMO systems and introduced the 2D Fourier domain line search MUSIC algorithm. Krishnaveni et al. [19], Devendra and Manjunathachari [20], and Barua et al. [21] have surveyed some directions of arrival methods. Many other AoA estimators have also been developed, which focus on different array structures and faster processing speeds. Some examples are given in [22–28].

There are also some AoA estimation methods that are based on compressive sensing (CS) theory [29–31]. Gurbuz et al. [32, 33] applied CS to estimate acoustic wave AoA by focusing on one receiving channel sampling at Nyquist rate and the other channels sampling at CS rate. Using the target bearing as a sparse vector, Cevher et al. [34] demonstrated multielement circular acoustic sensor arrays to obtain the bearings of multiple sources by applying an l_1 -norm minimization solution called the Dantzig selector [35]. Wu and Elangage [36] introduced a CS-based ultra-wideband 2D AoA estimation scheme that can estimate AoA of the SOI from 2 to 18 GHz without any a priori knowledge of the intercepted signals. Other examples of treating AoA estimation as a sparse recovery problem can be found in [37–40]. Bayesian CS- (BCS-) based AoA estimation was also developed in [41–43]. The key advantage of the BCS AoA estimator is its ability to estimate signal AoA with few measured data from each element in the array.

To estimate the AoA of SOI in a nonstationary environment and to avoid having to form a signal covariance matrix, the Direct Data Domain (D3) method was introduced [44–47]. Using the D3 method and the concept of signal cyclostationarity, Sarker et al. [48] introduced a method that can handle a number of signals along with their various coherent and noncoherent multipaths and interferences, even when the number of signals exceeds the number of antenna elements. This was demonstrated using a 12-element uniform linear array. Some examples of using the D3 method for AoA estimations can be found in [49–54].

Most aforementioned methods and their usages on antenna arrays are suitable for narrow-band applications, as the array elements and their configurations closely relate to the signal wavelengths. Hence, they can be used mainly for AoA estimations in communication applications. Interferometry-based AoA measurement systems have been widely used in ESM systems for 2D AoA measurements in ultra-wide frequency ranges [2–4]. It is desirable to use the longest possible baseline in the array, to achieve low variance measurement results. However, longer baselines require higher signal-to-noise ratios (SNRs) in order to resolve the ambiguity using the associated trigonometric functions. In addition, even if the wideband antenna elements, such as cavity-backed spiral antennas (CBSA), are used in the five-element array in [2], the spacing of the short baseline in the array is chosen to be less than half of the wavelength of the highest frequency of interest. As a result, several different five-element interferometers are required to cover a wide operational frequency range. This results in a large antenna array footprint. Pasala et al. [5] introduced a three-element interferometer array that used multimodes in the elements

to avoid the short baseline required in the conventional five-element array configuration. The long baseline (larger array footprint) is still required to resolve the ambiguity. However, these large-footprint arrays are problematic for small airborne platforms, such as CubeSats (U-class spacecraft) [55], small unmanned aerial vehicles [56, 57], and drones.

In this paper, we propose a novel 2D angle-of-arrival (AoA) estimator for ESM applications from 6 to 18 GHz in low SNR environments with frequency-independent performance, when the SNR and the required estimation accuracy are given. This includes the following contributions:

- (i) A 2D 7-element compact nonuniformly spaced array (NSA) is designed with CBSA elements operating from 6 to 18 GHz, which has an array footprint that is smaller than a circle having a 41.4 mm radius.
- (ii) A 2D AoA measurement system applies the D3 method on the measured time-domain data (snapshots) from the 7-element NSA. This includes the following:
 - (a) A 2D data transformation from the 7-element NSA-measured data to a 2D isotropic-element planar array (IEPA) data is introduced in order to use the NSA data in the D3 method for AoA estimation, and six different 2D IEPAs are considered.
 - (b) Using 2D IEPA steering vector (SV) and the results derived from the D3 method, a new objective function is introduced for searching the AoA of the SOI solution in both azimuth (Az) and elevation (El) angles. This (1) avoids having to solve the ambiguity problem encountered in interferometric arrays and (2) gives the estimator a frequency-independent performance.
 - (c) Using a 3D icosphere, a 2D-angle grid is introduced to give a near-uniform angular distribution in the field of view (FOV) of the 7-element NSA. On this grid, the data-transformation matrix database and SVs of IEPAs are precalculated at a list of preselected frequency points and stored in a computer prior to AoA estimations. Hence, the estimator can be used for ESM applications without a priori knowledge of the SOI.
- (iii) Since the focus of this development is ESM application in low SNR environments, different SNR levels are studied with four different commonly used radar waveforms. They are the following: (1) a 13-chip Barker-coded waveform, (2) a 20-chip two-valued frequency-coded waveform [58], (3) a 16-chip poly-phase-coded waveform, and (4) an ultra-wideband (100 MHz chirp) frequency-modulated continuous waveform (FMCW).

In addition to the above contributions, the findings of this study are highlighted as follows:

- (i) The preferred IEPA for this application has a circular-shape, which also has the least number of elements.
- (ii) The new AoA estimation scheme shows frequency-independent performance defined by the probability of AoA estimation, when the required AoA estimation accuracy is specified for a fixed SNR. This performance results from using the nonuniformly (nonregularly) spaced CBSA array, applying the 2D data transformation to convert measured data from the NSA to a planar array and then using the new 2D AoA searching method introduced in this paper.
- (iii) In general, the more snapshots used in AoA estimation, the better the accuracy that can be achieved or the higher the probability of AoA estimation for a given SNR and desired accuracy.
- (iv) The estimator can estimate 2D AoA using few snapshots in a high SNR environment.

The paper is organized as follows: The 7-element NSA design is presented in Section 2. The AoA estimation algorithm for a planar array with isotropic radiators in free space is then discussed in Section 3. Section 4 presents a 2D data transformation that maps the time-domain sampled data (or snapshots) from the 7-element NSA to the data of an IEPA, so that the D3 method introduced in Section 3 can be applied. Section 5 discusses how to apply the AoA estimation method to an ESM system with ultrawide frequency range without a priori knowledge of the frequency of the SOI. The simulation results and discussion are presented in Section 6. The last section gives the conclusions and future work. There are four appendixes in this paper. Appendix A defines the six IEPAs. A description of the 2D-angle grid on the vertices of a unit icosphere is given in Appendix B. Four commonly used radar waveforms with their parameters are given in Appendix C. Appendix D explains the reasons why the estimator has frequency-independent performance with respect to the probability of AoA estimation mentioned above.

2. Design of a 7-Element 6–18 GHz NSA

Figure 1 illustrates the 7-element CBSA array, and Figure 2 shows nonuniform interelement spacings. The element locations in XY -plane are given in Table 1. The reasons for choosing the element locations are to ensure that (1) element spacings in X and Y directions are as close to half the wavelength of the highest operational frequency as possible, (2) the distances between adjacent element centers are bigger than the diameter of the CBSA element, and (3) the overall array footprint is as small as possible. As a result, the average element spacing in both X and Y directions is about 8.44 mm, which is a little bigger than half of the free-space wavelength at 18 GHz, i.e., 8.33 mm. The element used in the NSA is a commercial-off-the-shelf 6 to 18 GHz CBSA with 24.4 mm diameter. In addition to ultra-wideband operational frequency band of the array, another advantage of using the CBSA element is the possibility of neglecting the performance changes caused by the mutual coupling

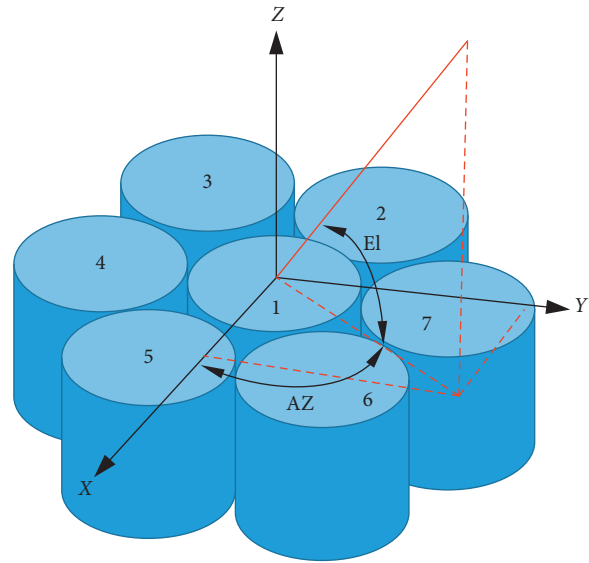


FIGURE 1: A 3D illustration of the 7-element CBSA NSA. The phase-reference center is at the first element center.

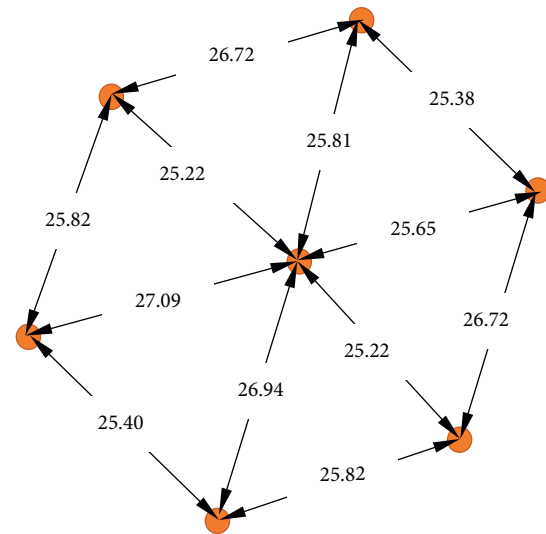


FIGURE 2: The top view of element centers with interelement spacings (unit is in mm).

TABLE 1: Antenna element locations.

Element	px_n (mm)	py_n (mm)	pz_n (mm)
1	0.0	0.0	0.0
2	24.74	6.79	0.0
3	6.79	24.74	0.0
4	-18.75	16.87	0.0
5	-25.90	-7.94	0.0
6	-7.94	-25.90	0.0
7	16.87	-18.75	0.0

between adjacent elements in the array [59]. It is mainly because the element has about 80° to 100° 3 dB beamwidth in its broadside and very low radiation, when El-angle approaches 0° . Examples of measured antenna radiation can be found in [60].

3. AoA Estimation from a Planar Array with Isotropic Elements

Before discussing the AoA estimation algorithm for the NSA, this section briefly presents the AoA estimation algorithm for a planar array with isotropic elements, which is the 2D version of the development given in [48]. Although, in this study, the D3 method was applied to 2D planar arrays given in Appendix A, the AoA estimation method proposed in this section can also be applicable to other sparse array structures, such as 2D nested array [22].

3.1. SOI Representation. The intercepted signal output at the n^{th} antenna element in an IEPA can be expressed as a complex envelop signal:

$$x_n(t) = A_n(t)e^{(j2\pi f_c t + \phi)} + \aleph(t) + \Omega, \quad (1)$$

where A , f_c and ϕ are the amplitude, frequency and initial phase of the waveform of the SOI, respectively. \aleph is the white Gaussian noise added by the receiver. In the following simulations, it is added to the signal in each receiving channel based on the signal-to-noise ratio (SNR) defined in each simulation and the power of the SOI. $n = (1, 2, \dots, NN)$ and NN is the total number of elements in the IEPA. Ω represents other unwanted signals, such as jamming signals. Since signal collision or pulse collision is not considered in this study, Ω is excluded in the latter equations. If the received signal in (1) is sampled at a set of time instants $m = (1, 2, \dots, M, M + 1)$, the collected data can be expressed as

$$x_n(m) = A_n(m)e^{(j2\pi f_c m \cdot dt + \phi)} + \aleph(m), \quad (2)$$

where dt is the temporal sampling interval.

If the phase reference is at the center element of the array, and it is located at the origin of the coordinate system, the received signal of the m^{th} snapshot at the n^{th} element is

$$x_n(m) = A_n(m)e^{\{j2\pi/\lambda\} [px_n \cos(\text{El})\cos(\text{Az}) + py_n \cos(\text{El})\sin(\text{Az}) + pz_n \sin(\text{El})]} + \aleph(m), \quad (3)$$

where λ is the SOI free-space wavelength, (Az, El) is the SOI incident direction, and (px_n, py_n, pz_n) are given in Table 1.

3.2. Cyclostationarity of the SOI. The cyclostationarity is a nonlinear transformation operating on a signal, and it generates finite-strength additive sine-wave components that result in spectral lines [61]. A signal $x(t)$ is assumed to

be having a cyclostationary feature with cycle-frequency η , if and only if the product $x(t) \cdot x(t - \tau)$, for some delay τ , shows a spectral line at frequency η .

The signals to be detected in our problem are cosine-wave based signals, for example,

$$A(t)\cos(2\pi f_c t). \quad (4)$$

Let us assume the second-order nonlinear transformation, which is equivalent to multiplying the signal with its shifted version or simply to square the SOI; the new signal has a cycle-frequency η that can be

$$A^2(t) \cdot \cos^2(2\pi f_c t) = \left(\frac{A^2(t)}{2}\right)\cos(2\pi\eta t) + \text{constant}, \quad (5)$$

$$\eta = 2f_c, \quad (6)$$

where it assumes that the delay or shift is zero. The complex envelope form of (5) is

$$A^2(t)e^{j2\pi\eta t}. \quad (7)$$

In many applications, the SOI cyclostationary information is a priori known information, for example, the cycle-frequency of the carrier frequency between two communication sites. However, in ESM, the intercepted signal frequency (f_c) has to be estimated.

3.3. D3-Based AoA Method for an IEPA. First, let us apply a second-order nonlinear transform to the signal in (2) as we did in (5) and then regroup the transformed signals into the signal with cycle-frequency and other frequency components. We have

$$x_n^2(m) = A^2(m)e^{j2\pi\eta m \cdot dt} + \text{Others}, \quad (8)$$

where Others includes other frequency components not around $\eta = 2f_c$ and noise. Note that, in this study, the signal collision is not considered; i.e., the signal to be processed only has one carrier in the current RF receiver band, even though the receiver can be tuned from 6 to 18 GHz. Using $M + 1$ temporal snapshots from each element of an NN -element IEPA, the following matrix equation can be constructed. The detailed derivation and discussion are given in Chapter 7 of [48] for a linear array case. Here, we extend it to the 2D planar array application:

$$\mathbf{Z}_{(NN+1) \times M} \mathbf{W}_{M \times 1} = \mathbf{E}_{(NN+1) \times 1}, \quad (9)$$

where

$$\mathbf{Z} = \begin{bmatrix} 1 & \dots & e^{j2\pi(M-1)\eta \cdot dt} \\ x_1^2(1) - x_1^2(2)e^{-j2\pi\eta \cdot dt} & \dots & x_1^2(M) - x_1^2(M+1)e^{-j2\pi\eta \cdot dt} \\ \vdots & \dots & \vdots \\ x_{NN}^2(1) - x_{NN}^2(2)e^{-j2\pi\eta \cdot dt} & \dots & x_{NN}^2(M) - x_{NN}^2(M+1)e^{-j2\pi\eta \cdot dt} \end{bmatrix}, \quad (10)$$

\mathbf{W} is the unknown weight vector that can be detailed as

$$\mathbf{W} = \begin{bmatrix} w_1 \\ w_2 \\ \vdots \\ w_M \end{bmatrix}, \quad (11)$$

and \mathbf{E} is the excitation vector, given as

$$\mathbf{E} = \begin{bmatrix} C \\ 0 \\ \vdots \\ 0 \end{bmatrix}. \quad (12)$$

The length of column vector \mathbf{E} is $NN + 1$, and the constant C can be arbitrarily selected and it also satisfies the following relation with weight vector:

$$C = \sum_{m=1}^M w_m e^{j2\pi(m-1)\eta \cdot dt}. \quad (13)$$

However, (13) is not a necessary condition since the constant C gets factored out in the final AoA computation. Equation (13) expresses that the sum of the weights produces a gain factor C , when they are applied to the SOI at the cycle-frequency. The Moore–Penrose pseudo-inverse was used to solve (9) in order to obtain \mathbf{W} , which has $\|\mathbf{W}\|_2 = C/\sqrt{M}$.

The elements from the second row and after in (10) can be written as $x_n^2(m) - x_n^2(m+1)e^{-j2\pi\eta \cdot dt}$, which tells that the SOI component at the cycle-frequency $\eta = 2f_c$ is removed from the matrix elements. Thus, the weight vector \mathbf{W} obtained from (9) minimizes the noise and other frequency components and simultaneously satisfies (13). This is one of the reasons why the algorithm has the ability to measure weak signals from noise and can give a good estimation of the AoA of the SOI.

The advantages of (9) are as follows: (1) the temporal data are directly used without being converted to frequency domain, and no covariance matrix is required and (2) the number of time-domain snapshots can be very small, e.g., $M + 1 = 2$, in high SNR cases. Hence, it can be used in dynamic signal environments with good SNR.

3.4. Detecting SOI by Estimating Its AoA Using IEPA. For a given element n in an IEPA, when the $(n + 1)^{\text{th}}$ row of matrix \mathbf{Z} in (10) is multiplied with the weight-vector \mathbf{W} , one has

$$\sum_{m=1}^M \{x_n^2(m) - x_n^2(m+1) \cdot e^{-j2\pi\eta \cdot dt}\} w_m = 0. \quad (14)$$

From (14), considering $w_m \neq 0$, $e^{j2\pi\eta \cdot dt} \neq 0$, and (13), the following equation can be derived:

$$\frac{1}{C} \sum_{m=1}^M x_n^2(m) w_m = e^{\{j4\pi/\lambda_{\text{est}}\} [px_n \cos(\text{El}) \cos(\text{Az}) + py_n \cos(\text{El}) \sin(\text{Az})]}, \quad (15)$$

where it is assumed that $pz_n = 0$, $\lambda_{\text{est}} = (c/f_{c_{\text{est}}})$, and c is the speed of light in free space. Equation (15) unveils some important results including the following:

- (i) The operation $\sum_{m=1}^M x_n^2(m) w_m$ means that the weight vector applies a filter to the squared values of snapshots.
- (ii) The sum of the filtered data in the Item-1 above only relates to the AoA of SOI.
- (iii) The weights only can be used to filter the current set of squared values of snapshots used in (9) to minimize the undesired signal at the output. If snapshots are changed, the weights obtained from (9) will be changed accordingly, but the sum will not be changed.

The Item-3 in the above discussion reflects the dynamic nature of this method, where the processing only deals with the current set of snapshots fed to (9).

Since (15) uses the n^{th} element's measured snapshots and has two unknowns (Az, El), the solution can be calculated using any two elements in the array to form two equations from (15). However, we are going to introduce a new approach to find AoA in the following sections, which uses the IEPA SV and a 2D searching method. The advantage of the new approach is the ability to avoid having to pick answers from an unlimited number of solutions of inverse trigonometric functions and the possibility of finding AoA solution with no dependency on frequency at a fixed SNR. The reason for the frequency-independent behavior is discussed in Appendix D.

This new AoA searching method is the second important reason that explains why our scheme can robustly measure the weak signals and how it can offer a good estimation of AOA of the SOI. The novelty of this approach is using all the NN elements together for the AoA solution, rather than using a few elements in the array to find the AoA solution from inverse trigonometric functions.

3.5. IEPA Steering Vector and Objective Function. If an IEPA is located at the origin of the Cartesian coordinate system, its SV for an incoming plane wave is

$$\mathbf{sv} = \begin{bmatrix} e^{j\hat{\mathbf{k}} \cdot \vec{\mathbf{r}}_1} \\ e^{j\hat{\mathbf{k}} \cdot \vec{\mathbf{r}}_2} \\ \vdots \\ e^{j\hat{\mathbf{k}} \cdot \vec{\mathbf{r}}_n} \\ \vdots \\ e^{j\hat{\mathbf{k}} \cdot \vec{\mathbf{r}}_{NN}} \end{bmatrix}, \quad (16)$$

where $\hat{\mathbf{k}}$ is the wave vector and $\vec{\mathbf{r}}_n$ is the displacement vector from the signal source to the n^{th} element in the array.

If the center element of the array is located at the origin and its phase is used as the phase reference, then the array SV becomes

$$\mathbf{sv}(az, el) = \begin{bmatrix} e^{j(2\pi/\lambda)[px_1 \cos(el)\cos(az) + py_1 \cos(el)\sin(az)]} \\ e^{j(2\pi/\lambda)[px_2 \cos(el)\cos(az) + py_2 \cos(el)\sin(az)]} \\ \vdots \\ 1 \\ \vdots \\ e^{j(2\pi/\lambda)[px_n \cos(el)\cos(az) + py_n \cos(el)\sin(az)]} \\ \vdots \\ e^{j(2\pi/\lambda)[px_{NN} \cos(el)\cos(az) + py_{NN} \cos(el)\sin(az)]} \end{bmatrix}. \quad (17)$$

The SV at the center element is equal to one. It is also assumed that all the elements have the same locations in z direction.

Comparing (17) with (15), one can find that in order to estimate the AoA (Az, El), a 2D searching method can be used to find (az_e, el_e) by

$$\min_{\substack{az=az_e \\ el=el_e}} \sum_{n=1}^{NN} \left| sv_n^2(az, el) - \frac{1}{C} \sum_{m=1}^M x_n^2(m)w_m \right|^2, \quad (18)$$

where sv_n^2 is the square of sv_n at the n^{th} isotropic element in (17) with $\lambda = \lambda_{\text{est}}$, which is the same as the right side of (15). The details of the searching method will be given in Section 5.

4. AoA Estimation Using the 7-Element NSA-Measured Snapshots

This section discusses how to use snapshots from the 7-element NSA to estimate the AOA of the SOI by taking advantage of the 2D D3-based AoA method discussed in the last section.

4.1. 2D Transformation Matrix to Convert 7-Element NSA-Measured Data to IEPA Data in Free Space. Consider a setup for the 7-element NSA calibration. A far-field source at frequency f_c is placed along the direction $(az(p), el(p))$, and the measured phasor voltages at 7 output ports can be expressed as $y_n(p, f_c)$ ($n = 1, 2, \dots, 7$). Here, p indicates the source at the p^{th} direction. If this source is moved in total P directions and at each direction, one collects the phasor voltage at each element, a measured data matrix $\mathbf{Y}_{7 \times P}(f_c)$ can be obtained. Then, replacing the NSA by an NN -element IEPA and performing the same measurement, the output phasor voltage matrix from the planar array $\mathbf{U}_{NN \times P}(f_c)$ can be created. In reality, instead of making measurement, it can be calculated, since the isotropic element in free space does not exist.

The goal is to find the best-fit data-transformation matrix that satisfies

$$\mathbf{T}_{NN \times 7}(f_c) \cdot \mathbf{Y}_{7 \times P}(f_c) = \mathbf{U}_{NN \times P}(f_c). \quad (19)$$

This equation can be solved using the least square method. It is achieved by minimizing the following function:

$$\min_{\mathfrak{S}} \left\| \mathbf{U}_{NN \times P}(f_c) - \mathbf{T}_{NN \times 7}(f_c) \cdot \mathbf{Y}_{7 \times P}(f_c) \right\|, \quad (20)$$

where \mathfrak{S} is the best-fit transformation matrix. In order to have a unique solution of (20), the number of P directions must be greater than or equal to the number of antenna elements in the planar array.

For frequency f_c , the transformation matrix (\mathfrak{S}) has to be stored in computer memory. Then, during the operation, snapshots $\mathbf{Y}_{7 \times 1}(m, Az, El, f_c)$ from the NSA can be converted to snapshots of the NN -element IEPA by

$$\mathbf{U}_{NN \times 1}(m, Az, El, f_c) = \mathfrak{S}_{NN \times 7}(f_c) \mathbf{Y}_{7 \times 1}(m, Az, El, f_c), \quad (21)$$

where the incident direction (Az, El) of SOI should be within the limits of those directions during the calibration, but not necessary to be one of the P directions. This is called the off-grid case. After that, the AoA of SOI can be estimated using the algorithm discussed in the previous section.

Note that different frequencies f_c have different transformation matrices. Obtaining the transformation matrices for the 6–18 GHz radar ESM applications without a priori knowledge of the frequency of SOI is discussed in Section 5.

4.2. Discussion. The calibration method and the data-transformation given in (19) to (21) can be applied to planar arrays of any size and any shape. Six different IEPAs are used in this study to demonstrate the approach. These arrays are presented in Appendix A.

In real applications, the data-transformation introduced in this section

- (i) eliminates the nonuniformity in the real array, which means it transfers a NSA into a regular-spaced IEPA
- (ii) converts a 3D real antenna problem into an isotropic-element regular-spaced array problem in free space
- (iii) takes into account the mutual coupling between elements in a real array, when the \mathbf{Y} matrix is measured
- (iv) removes the inconsistency among receiver channels, when the NSA elements are connected to RF receivers
- (v) can remove the electromagnetic interferences by the presence of near-field scatterers, for example, the body of the platform, if the calibration measurement is performed with a platform in a big microwave anechoic chamber

5. Application of the Method to ESM

In the discussion of Sections 3 and 4, although the snapshots measured in time domain are used in (10) and (15) to calculate the weight vector in (11), the method still requires

the carrier frequency of the intercepted radar signal for the following purposes:

- (i) To obtain the cycle-frequency
- (ii) To determine the IEPA SV
- (iii) To determine the data-transformation matrix, which has to be obtained and stored in computer memory prior to AoA measurements

Unfortunately, in radar ESM applications, the SOI carrier frequency has to be estimated ($f_{c_{est}}$). This section introduces an approach to deal with this problem.

First, let us discuss how to obtain the precalculated SV database and the transformation matrix \mathfrak{F} database for a given IEPA based on the 2D-angle grid introduced in Appendix B. Then, we give the detailed steps of using these databases for AoA estimations.

5.1. Precalculated SV Database and \mathfrak{F} Database. From 6 to 18 GHz, total 2401 equal-spaced frequency points (f_{c_i}) are preselected to develop the databases, so that the frequency step is 5 MHz. For an IEPA, the SV database can be written as

$$\text{squared_SV}(f_{c_i}, z) = \text{sv}_n^2(\text{az}_z(p), \text{el}_z(p), f_{c_i}), \quad (22)$$

where $n = 1, 2, \dots, NN$ and $i = 1, 2, \dots, 2401$. $z = 1, 2, \dots, 36$, and p is the p^{th} direction in the z^{th} angle zone shown in Figure 17(a) in Appendix B. $P_{\text{total}} = \sum_{z=1}^{36} P(z) = 29495$, where $P(z)$ is the total directions in the z^{th} angle zone.

The \mathfrak{F} matrix used in (21) is developed in each angle zone at every frequency (f_{c_i}) and can be written as

$$\mathfrak{F}_{NN \times 7}(f_{c_i}, z). \quad (23)$$

Basically, the number of directions P in (19) is replaced by $P(z)$ in each angle zone. Hence, for each planar array, at every frequency point and within each angle zone, a pair of precalculated squared-SV and \mathfrak{F} matrix is saved in the computer memory.

5.2. AoA Measurement without a Priori Knowledge of the Carrier of the SOI. During the AoA measurement, once the $f_{c_{est}}$ is obtained from the ESM system, the closest frequency point (f_{c_i}) in ($f_{c_i}, i = 1, 2, \dots, 2401$) can be found and the corresponding squared-SV(f_{c_i}, z) and $\mathfrak{F}_{NN \times 7}(f_{c_i}, z)$ are used in the AoA estimation. To search AoA solution, the second term in (18) obtained by the D3 method is compared with the first term at each direction defined by the 2D-angle grid in Figure 17(a) in Appendix B through 36 angle zones. Then, the direction that gives the minimum sum value in (18) is used as the solution.

6. Simulation Results and Discussion

In this section, the simulation results are first presented based on the probability of AoA measurement versus SNR under the conditions of (1) different RMSE requirements

and (2) using different ($M + 1$) snapshots during estimations. The RMSE of each AoA estimation is defined as

$$\sqrt{\frac{(\Delta \text{Az})^2 + (\Delta \text{El})^2}{2}}, \quad (24)$$

where ΔAz and ΔEl are the measurement errors in Az- and El-angle, respectively. Then, the estimation errors in Az- and El-angles are discussed. Finally, the results of the use of a small number of snapshots for AoA estimation under high SNR conditions are also shown.

Simulation cases consist of the data which are processed by the six planar arrays on four different waveforms using different number of snapshots ($M + 1$) that varies from 2 to 1025. In each case,

- (i) A section of $M + 1$ consecutive snapshots is sent to AoA calculation. The starting point of a section of $M + 1$ data is randomly selected within a pulse of different waveforms discussed in Appendix C.
- (ii) There is a total of 100000 AoA estimations.
- (iii) The incident wave in each AoA estimation is generated as follows:
 - (a) The carrier frequency is uniform-randomly picked in [6, 18] GHz.
 - (b) The SNR of each processed signal is uniform-randomly chosen in [-20, 20] dB. It is assumed that the seven receivers add the same noise power to the received signals. The noise power is calculated based on the received signal power, and the noise has white Gaussian distribution.
 - (c) The incident direction in off-grid case is also uniform-randomly selected in the FOV.

6.1. Probability of AoA Estimation

6.1.1. Comparison with Different IEPAs. Tables 2–5 provide the SNRs that yield 50% or better probability of AoA estimation using 129, 257, 513, and 1025 snapshots, respectively, from the six different arrays (described in Appendix A) under different estimation accuracy requirements. In these tables, the values in bold, but not italicized, show the lowest SNR in a group of 6 SNRs produced by the 6 planar arrays, and the bold italic and normal italic values indicate the largest and the second largest SNRs in a data group, respectively. An IEPA with a lower SNR in a group means that it has a better capability of measuring AoA than the arrays with higher SNRs. This is because the array can estimate AoA of weaker signals than the rest of arrays which need stronger signals for the same accuracy.

From these tables, one can observe that Array-3 has 41 out of 64 values given in bold and Array-5 scores 21. This indicates that Array-3 is the best array among the 6 planar arrays to give a good AoA estimation, and Array-5 is the next to Array-3. Note that both of these two arrays are circular-shaped planar arrays with different interelement patterns.

On the other hand, one can see that Array-6 and Array-1 share the most bold-italicized and italic values. Array-6 has 50

TABLE 2: SNR (dB) values when arrays can produce 50% correct results using 129 snapshots under different estimation accuracies.

	RMSE $\leq 1^\circ$ (Array-1, 2, 3, 4, 5, 6)	RMSE $\leq 2^\circ$ (Array-1, 2, 3, 4, 5, 6)	RMSE $\leq 5^\circ$ (Array-1, 2, 3, 4, 5, 6)	RMSE $\leq 10^\circ$ (Array-1, 2, 3, 4, 5, 6)
WF-1	0.58/-0.94/- 1.00 /-0.42/-0.79/ 0.87	-2.30/-3.85/- 4.04 /-2.34/-3.50/- 2.02	-5.12/-6.56/- 6.74 /-5.27/-6.50/- 5.04	- 6.90 /-7.92/-7.79/-7.03/- 8.03 /-6.94
WF-2	0.71/-0.89/- 0.95 /0.28/-0.84/ 0.95	-2.16/-3.83/- 3.91 /-2.21/-3.65/- 1.81	-5.04/-6.43/- 6.62 /-5.01/-6.58/- 4.98	-6.89/-8.02/-7.87/-6.87/- 8.10 /-6.71
WF-3	0.63/-0.90/- 1.00 /0.57/-0.70/ 0.92	-2.19/-3.74/- 3.82 /-2.24/-3.63/- 1.96	-5.05/- 6.75 /-6.67/-5.18/-6.40/- 4.88	-6.97/-7.81/-7.85/-6.86/- 7.99 /-6.80
WF-4	0.81/-0.75/- 0.81 /0.48/-0.65/ 0.87	-2.11/-3.78/- 3.85 /-2.34/-3.61/- 1.88	-5.06/-6.69/-6.66/-5.07/- 6.70 /- 4.92	-6.91/-7.87/-7.68/-6.96/- 7.98 /-6.71

TABLE 3: SNR (dB) values when arrays can produce 50% correct results using 257 snapshots under different estimation accuracies.

	RMSE $\leq 1^\circ$ (Array-1, 2, 3, 4, 5, 6)	RMSE $\leq 2^\circ$ (Array-1, 2, 3, 4, 5, 6)	RMSE $\leq 5^\circ$ (Array-1, 2, 3, 4, 5, 6)	RMSE $\leq 10^\circ$ (Array-1, 2, 3, 4, 5, 6)
WF-1	-1.33/-2.95/- 3.13 /-1.58/-3.03/- 1.18	-4.03/-5.72/-5.71/-4.01/- 5.76 /- 3.88	- 6.80 /-8.13/- 8.38 /-6.86/-8.34/-6.83	-8.75/-9.56/-9.50/- 8.06 /- 9.58 /-8.48
WF-2	-1.26/-2.90/- 3.19 /-1.39/-2.67/- 1.16	-3.94/-5.55/- 5.76 /-4.12/-5.61/- 3.93	-6.85/-8.14/-8.27/-6.92/- 8.55 /- 6.59	- 8.43 /-9.50/-9.60/-8.62/- 9.69 /-8.67
WF-3	-1.28/-2.99/- 3.23 /-1.62/-2.88/- 1.20	-4.15/-5.74/- 5.86 /-4.36/-5.55/- 3.85	-6.86/-8.39/-8.22/-6.94/- 8.53 /- 6.70	- 8.54 /-9.56/-9.57/-8.58/- 9.81 /-8.60
WF-4	-1.12/-2.53/- 2.85 /-1.31/-2.62/- 0.95	- 3.38 /-5.25/- 5.59 /-3.94/-5.07/-3.63	-6.41/-7.98/-7.87/- 6.38 /- 8.28 /-6.43	-8.32/-9.36/- 9.51 /-8.26/-9.35/- 8.20

TABLE 4: SNR (dB) values when arrays can produce 50% correct results using 513 snapshots under different estimation accuracies.

	RMSE $\leq 1^\circ$ (Array-1, 2, 3, 4, 5, 6)	RMSE $\leq 2^\circ$ (Array-1, 2, 3, 4, 5, 6)	RMSE $\leq 5^\circ$ (Array-1, 2, 3, 4, 5, 6)	RMSE $\leq 10^\circ$ (Array-1, 2, 3, 4, 5, 6)
WF-1	-3.29/-5.00/- 4.99 /-3.36/-4.77/- 3.07	-5.68/-7.59/- 7.66 /-5.82/-7.47/-5.69	-8.47/-9.91/-9.87/-8.40/- 9.94 /- 8.38	-10.20/-11.33/-11.06/- 10.11 /- 11.37 /-10.29
WF-2	-3.30/-4.88/- 5.15 /-3.41/-4.84/- 2.97	-5.60/-7.39/- 7.68 /-5.66/-7.33/- 5.56	-8.37/-9.99/- 10.10 /-8.45/-9.04/- 8.18	-10.24/-11.17/-11.06/-10.28/- 11.20 /- 10.17
WF-3	-3.24/-5.01/- 5.04 /-3.32/-4.95/- 2.83	-5.76/-7.60/- 7.82 /-5.93/-7.38/- 5.64	- 8.41 /-9.88/- 9.99 /-8.55/-9.90/-8.53	-10.13/-11.12/-11.24/-10.06/- 11.28 /- 9.94
WF-4	-2.06/-3.71/- 3.72 /-2.23/-3.63/- 1.87	-4.54/-6.36/- 6.52 /-4.81/-6.19/- 4.24	-7.16/-8.91/- 8.92 /-7.37/-8.70/- 7.11	-8.92/-10.06/-10.03/-8.93/- 10.18 /- 8.87

TABLE 5: SNR (dB) values when arrays can produce 50% correct results using 1025 snapshots under different estimation accuracies.

	RMSE $\leq 1^\circ$ (Array-1, 2, 3, 4, 5, 6)	RMSE $\leq 2^\circ$ (Array-1, 2, 3, 4, 5, 6)	RMSE $\leq 5^\circ$ (Array-1, 2, 3, 4, 5, 6)	RMSE $\leq 10^\circ$ (Array-1, 2, 3, 4, 5, 6)
WF-1	-4.98/-6.72/- 6.99 /-5.18/-6.73/- 4.78	-7.46/-9.18/- 9.59 /-7.45/-8.97/- 7.27	-10.06/-11.73/- 11.79 /-10.25/-11.54/- 9.98	-11.87/-12.86/-12.56/-11.75/- 12.96 /- 11.66
WF-2	-4.83/-6.72/- 6.85 /-5.05/-6.49/- 4.71	-7.20/-9.01/- 9.11 /-7.39/-8.91/- 7.07	- 9.88 /-11.40/- 11.50 /-9.99/-11.48/-9.98	- 11.35 /-12.57/-12.60/-11.46/- 12.75 /-11.36
WF-3	- 4.88 /-6.66/- 6.91 /-5.21/-6.48/-4.92	-7.50/-9.11/- 9.43 /-7.43/-9.17/- 7.22	- 10.02 /-11.51/- 11.81 /-10.10/-11.58/-10.08	-11.84/-12.72/-12.73/-11.73/- 13.03 /- 11.69
WF-4	-0.63/-0.63/- 0.97 /0.71/-0.54/ 1.25	-3.57/-3.57/- 3.58 /-2.01/-3.27/- 1.77	-5.92/-5.92/-6.06/-4.66/- 6.34 /- 4.48	-7.50/-7.50/-7.48/-6.50/- 7.51 /- 6.31

bold-italicized and 7 italic values, and Array-1 has 11 bold-italicized and 38 italic values. This makes Array-6 to be the least favorite array among the 6 IEPAs, and Array-1 is the next. It is interesting to note that both Array-6 and Array-1 are rectangular-shaped planar arrays with different interelement patterns.

The above observation shows that our AoA estimation method prefers the planar array with symmetrical element distribution that can be seen from different Az-angles. In addition, Array-3 has the least number of elements. Hence it needs shorter computation time than the other arrays. Since Array-3 is the most favorable planar array out of the 6 arrays, the discussion in the rest of this paper uses the data produced by Array-3.

6.1.2. *Probability of AoA Estimation versus SNR.* Figures 3 and 4 show the results of probabilities of AoA estimation from Array-3 with estimation accuracies of 1° and 5° , respectively. Each subplot of these figures has 4 curves that present the results of 4 waveforms. From them, the following observations can be made:

- (i) When shorter snapshots are used in AoA calculations, i.e., subplots of in Figures 3(a) and (b) and Figures 4(a) and (b), the 4 curves of the 4 waveforms are very close to each other.
- (ii) When the number of snapshots is increased, the method still gives very close results for the first three waveforms, but the result of WF-4 starts deviating

from other results as shown in Figures 3(c) and (d) and Figures 4(c) and (d). Eventually, when $M + 1 = 1025$ in Figures 3(d) and 4(d), the results are worse than those in Figures 3(a-c) and Figures 4(a-c). This is because a longer sequence of FMCW snapshots covers a wider frequency range than those with a shorter sequence of snapshots. Hence it gives a bigger carrier frequency estimation error during calculations that degrades the probability of AoA estimation. Note that, in this study, a 100 MHz chirp signal has been used.

- (iii) In general, when more snapshots are used in the calculations, better estimation results can be achieved. This can also be clearly observed in Figure 5.

6.2. *AoA Estimation versus Frequency and SNR.* The probabilities of AoA estimation versus frequency and SNR are shown in Figures 6–9 for four different waveforms. From these figures, the following observations can be made:

- (i) For a given estimation accuracy, i.e., RMSE, at different frequencies, the method has about the same AoA estimation performance against the SNR. The explanation of this performance can be found in Appendix D.
- (ii) Again, the corresponding subplots in first three figures are basically similar, i.e., the method gives similar estimation performances for WF-1 to WF-3.

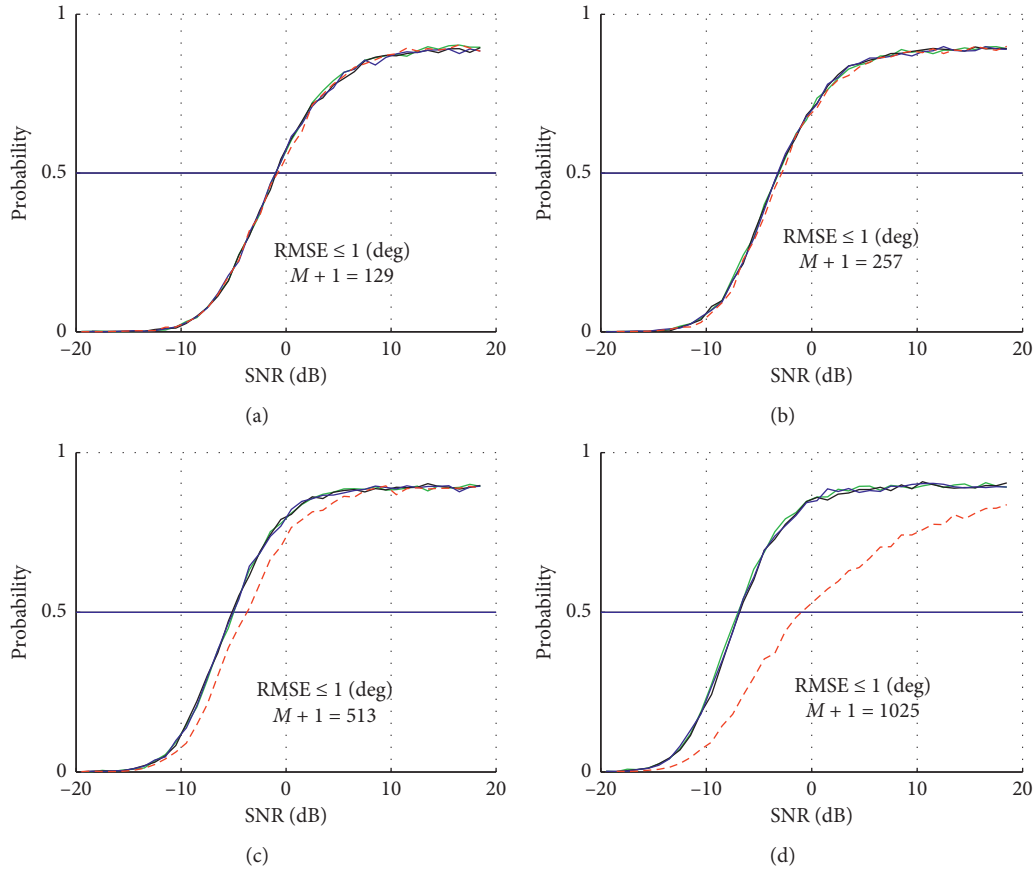


FIGURE 3: Probability of AoA measurement of Array-3, when $\text{RMSE} \leq 1^\circ$. Dashed line is WF-4 result.

- (iii) The subplots in Figure 9 are different from the corresponding subplots in the other figures, and the performances are not as good as in the other figures due to the reason discussed above.

6.3. Estimation Error Distributions in Az and El.

Figures 10–13 show the histograms of estimation errors of Az and El, when SNR is in different ranges with $M + 1 = 1025$. By comparing the left column and the right column in each figure, one can find the following:

- (i) The Az-error spreads wider than El-error, which indicates that the AoA estimation method produces better estimation results in El than in Az
- (ii) The lower the SNR, the wider the spread as expected
- (iii) Array-3 has almost the same estimation error distributions when it processes the first three waveforms

Tables 6–9 list the percentages of the absolute value of estimation errors that are less than or equal to 1° and 5° , when the SNR is in different ranges and $M + 1 = 1025$. The results shown in these tables confirm that the method has better estimation in El-angle than in Az-angle, which results from the definitions of Az- and El-angles.

Data in these tables also show the following:

- (i) When the SNR increases from $[0 \ 10]$ dB to $[10 \ 20]$ dB, the method does not improve much of its estimation accuracy.
- (ii) From Tables 6 and 7, when the SNR is greater than 0 dB, the estimation performance is mainly determined by the Az-angle estimation. The results in columns of “Both Az and El” and “Az” are very close to each other, and the results in columns of “El” are better than those in columns of “Az” for both $|\text{Er}| \leq 1^\circ$ and $|\text{Er}| \leq 5^\circ$ cases.
- (iii) From Table 8 ($-10 \text{ dB} \leq \text{SNR} \leq 0 \text{ dB}$), although the SNR is less than 0 dB, the overall estimation performance is slightly less than that of Az-angle estimation accuracy in both $|\text{Er}| \leq 1^\circ$ and $|\text{Er}| \leq 5^\circ$ cases. This means that the method starts producing bigger estimation errors in El. Nevertheless, the method still can produce better than 52% and 80% probabilities of AoA estimation with errors less than or equal to 1° and 5° , respectively, for the first three waveforms and better than 33% and 67% probabilities of AoA estimation with errors less than and equal to 1° and 5° for WF-4 with 513 snapshots.
- (iv) When the SNR is in $[-20 \ -10]$ dB, the method still has the capability of making some estimations and produce better than 20% probability of AoA estimation with errors within 5° for the first three waveforms.

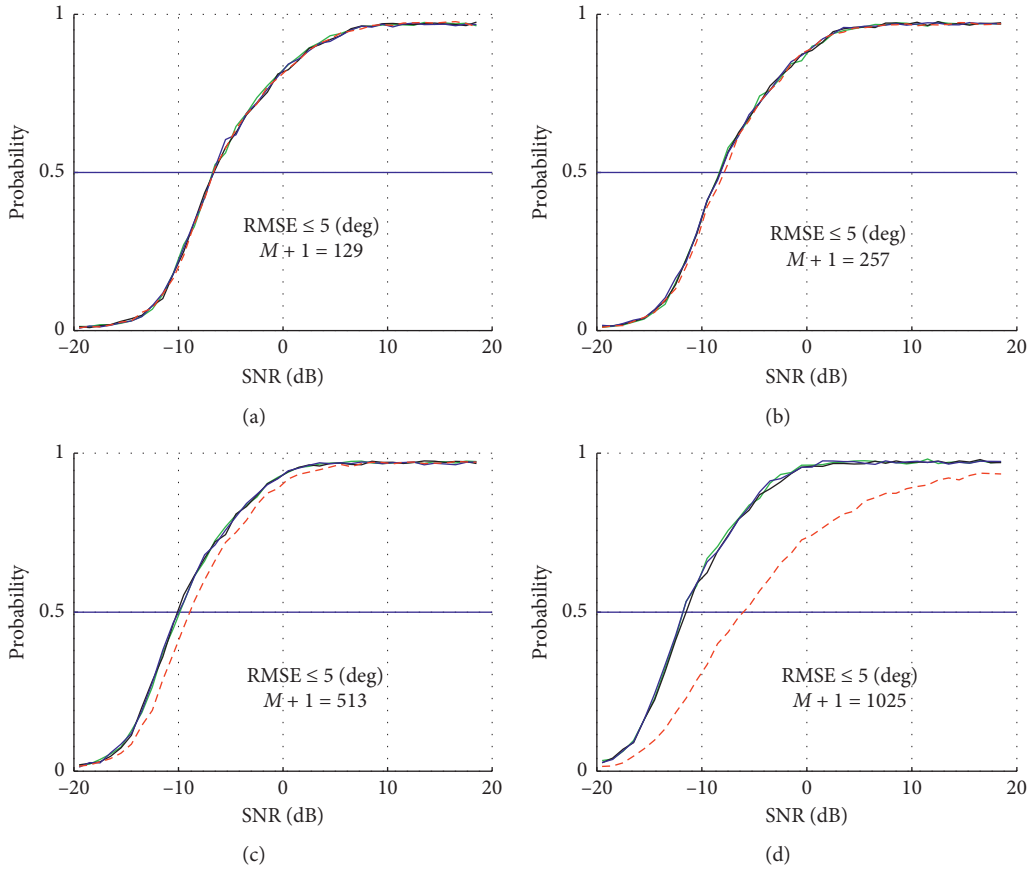


FIGURE 4: Probability of AoA measurement of Array-3, when $RMSE \leq 5^\circ$. Dashed line is WF-4 result.

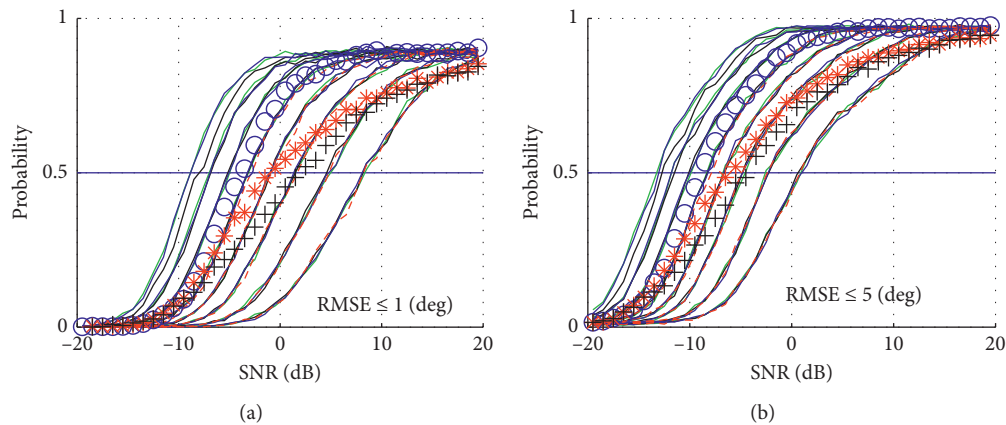


FIGURE 5: Probability of AoA measurement of Array-3 on 4 different waveforms with $M + 1 = 17, 33, 65, 129, 257, 513,$ and 1025 from right to left in each subplot. Each group of data has 4 curves related to 4 waveforms. ooooo, *****, and +++++ lines are the results of calculations on WF-4 using 513, 1025, and 2049 snapshots, respectively.

6.4. Probability of AoA Estimation Using Few Snapshots. To study the AoA estimation performance of the method in a good SNR environment, a total of 100000 SNR samples are randomly picked in $[-20 50]$ dB, and the results are shown in Figure 14. There are four groups of curves in each subplot of

the figure. They represent the use of 2, 3, 5, and 9 snapshots in the estimations. In each group of curves, there are four curves for four waveforms. Figure 14 shows that the method can have good probability of AoA estimation using just a few snapshots from the 7-element NSA. For example, with about

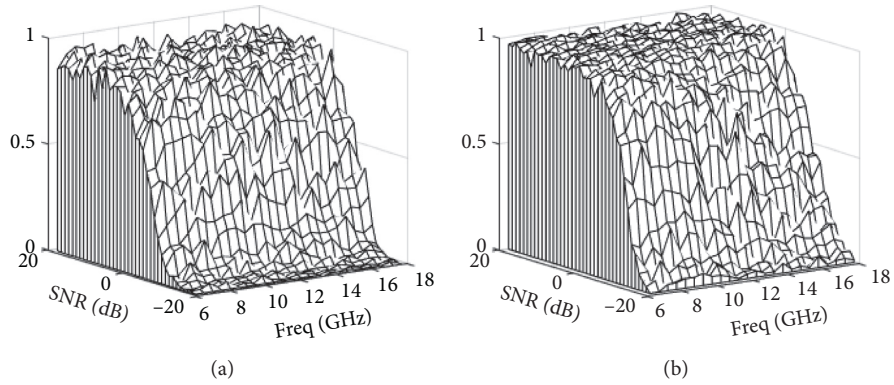


FIGURE 6: Array-3 probability of AoA estimation versus frequency and SNR: (a) $RMSE \leq 1^\circ$ and (b) $RMSE \leq 5^\circ$, when $M + 1 = 1025$ for WF-1.

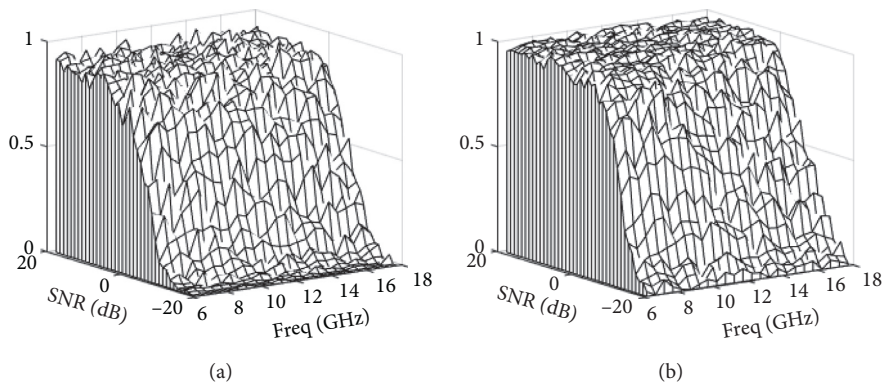


FIGURE 7: Array-3 probability of AoA estimation versus frequency and SNR: (a) $RMSE \leq 1^\circ$ and (b) $RMSE \leq 5^\circ$, when $M + 1 = 1025$ for WF-2.

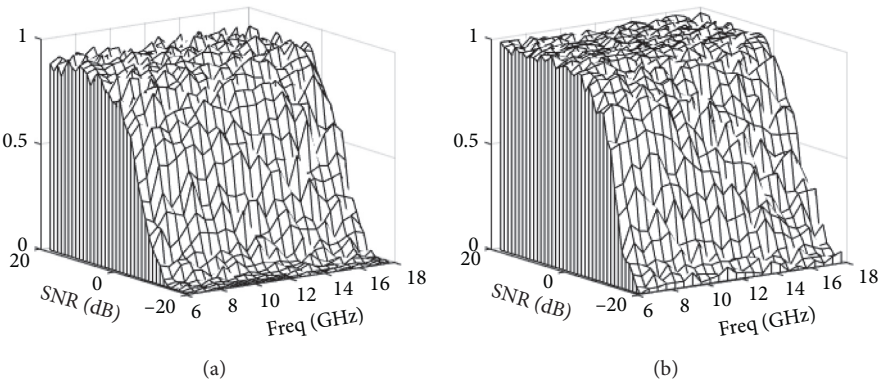


FIGURE 8: Array-3 probability of AoA estimation versus frequency and SNR: (a) $RMSE \leq 1^\circ$ and (b) $RMSE \leq 5^\circ$, when $M + 1 = 1025$ for WF-3.

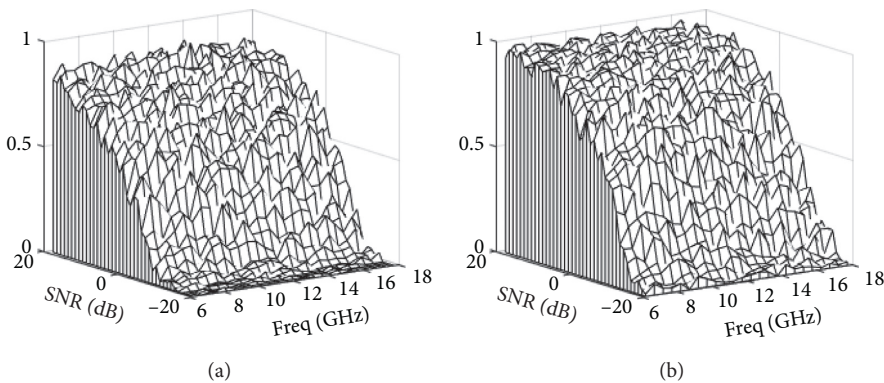


FIGURE 9: Array-3 probability of AoA estimation versus frequency and SNR: (a) $RMSE \leq 1^\circ$ and (b) $RMSE \leq 5^\circ$, when $M + 1 = 1025$ for WF-4.

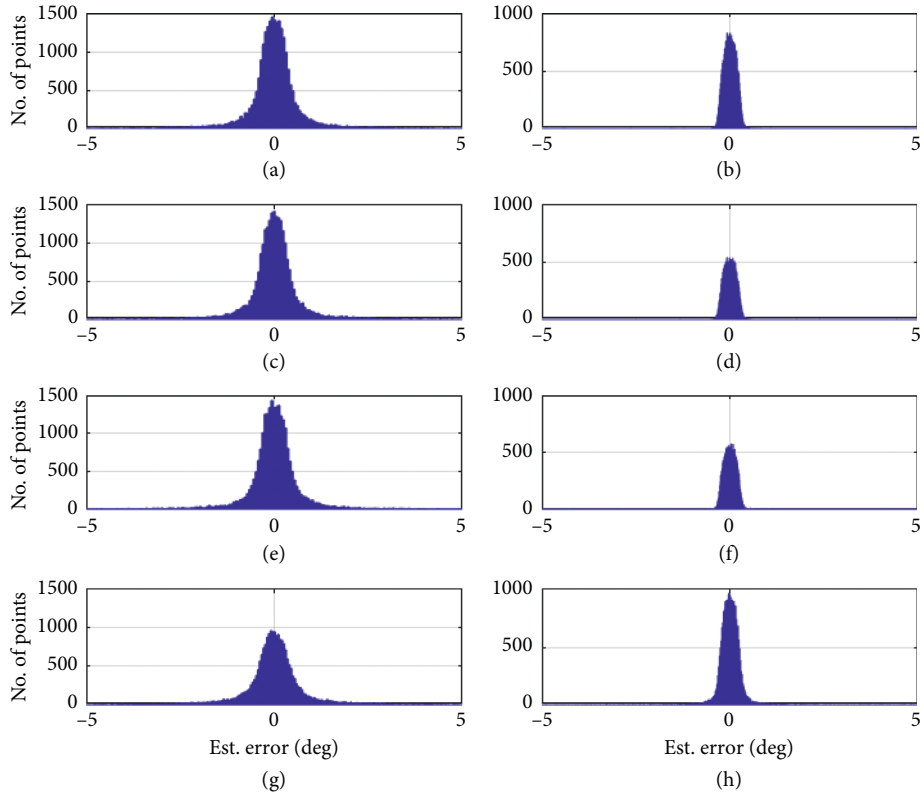


FIGURE 10: The histograms of Az (left column) and El (right column) estimation errors, when $10 \text{ dB} \leq \text{SNR} \leq 20 \text{ dB}$ with 1025 snapshots. (a, b) WF-1; (c, d) WF-2; (e, f) WF-3; (g, h) WF-4.

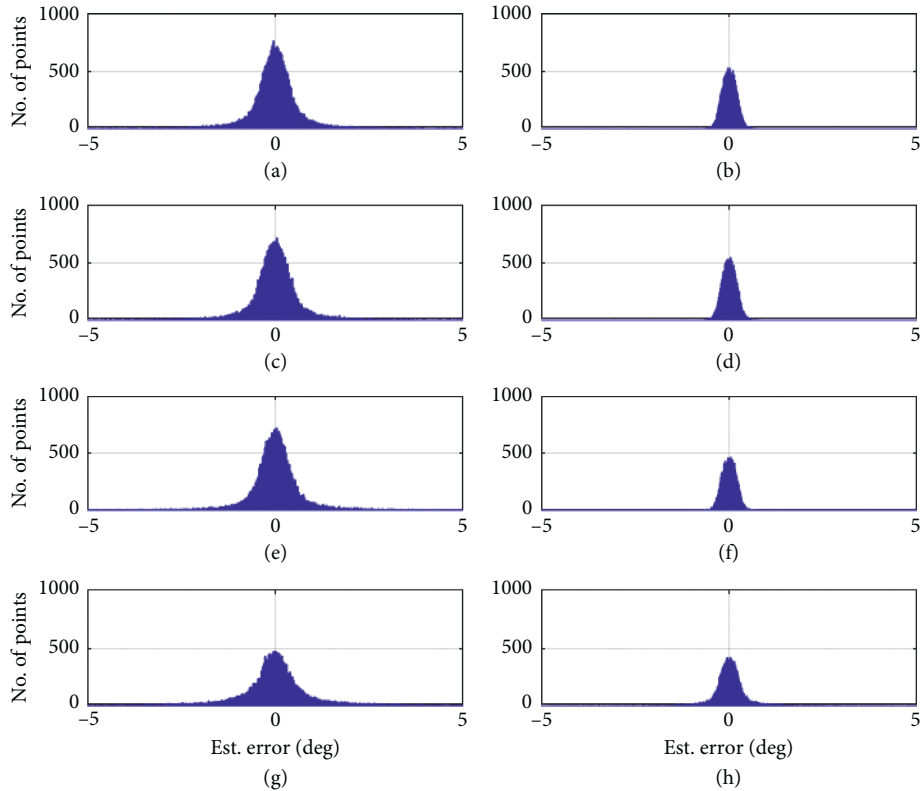


FIGURE 11: The histograms of Az (left column) and El (right column) estimation errors, when $0 \text{ dB} \leq \text{SNR} \leq 10 \text{ dB}$ with 1025 snapshots. (a, b) WF-1; (c, d) WF-2; (e, f) WF-3; (g, h) WF-4.

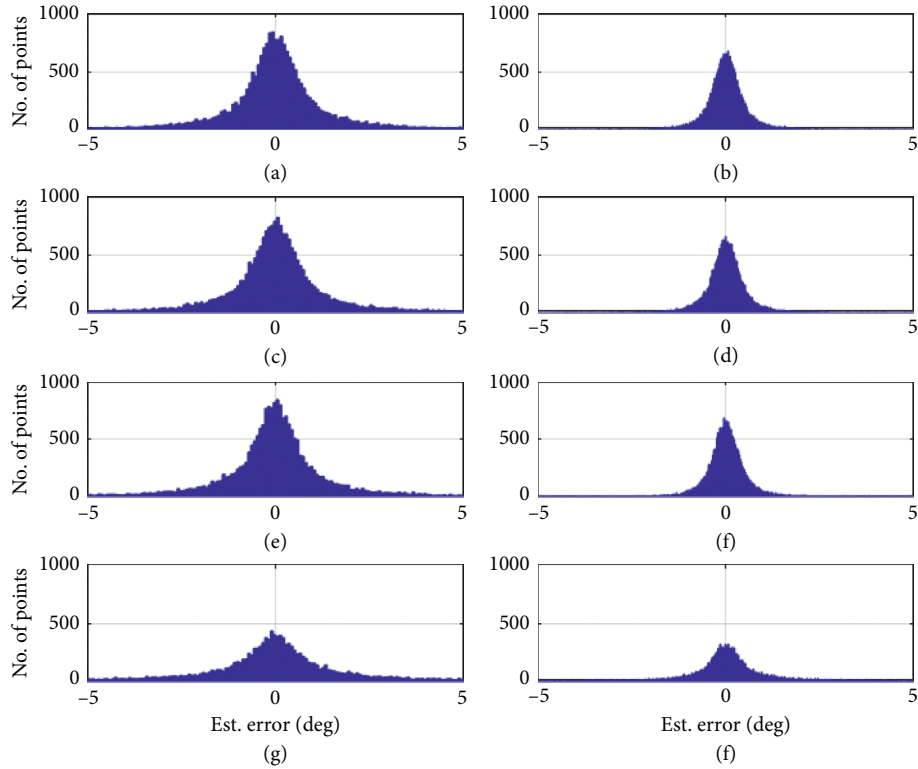


FIGURE 12: The histograms of Az (left column) and El (right column) estimation errors, when $-10 \text{ dB} \leq \text{SNR} \leq 0 \text{ dB}$ with 1025 snapshots. (a, b) WF-1; (c, d) WF-2; (e, f) WF-3; (g, h) WF-4.

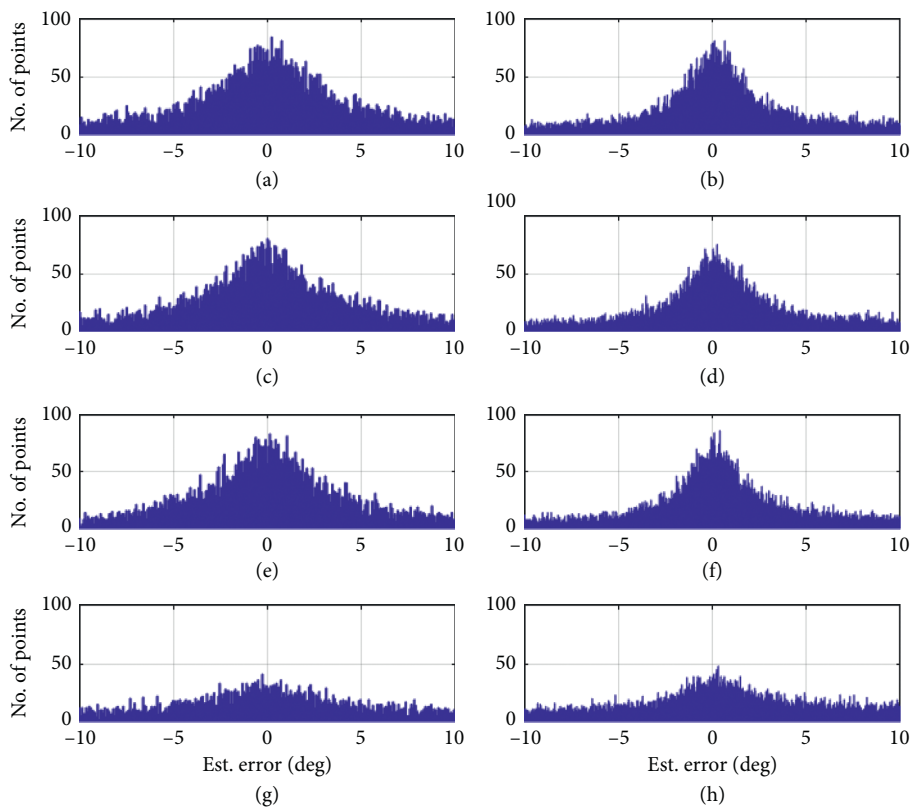


FIGURE 13: The histograms of Az (left column) and El (right column) estimation errors, when $-20 \text{ dB} \leq \text{SNR} \leq -10 \text{ dB}$ with 1025 snapshots. (a, b) WF-1; (c, d) WF-2; (e, f) WF-3; (g, h) WF-4.

TABLE 6: Array-3 probability of AoA estimation using 1025 snapshots ($10 \text{ dB} \leq \text{SNR} \leq 20 \text{ dB}$).

	Both Az and El, $ \text{Er} \leq 1^\circ$ $ \text{Er} \leq 5^\circ$	Az, $ \text{Er} \leq 1^\circ$ $ \text{Er} \leq 5^\circ$	El, $ \text{Er} \leq 1^\circ$ $ \text{Er} \leq 5^\circ$
WF-1	85.76% 96.42%	85.84% 96.50%	99.81% 99.87%
WF-2	85.66% 96.47%	85.76% 96.55%	99.79% 99.85%
WF-3	85.64% 96.37%	85.71% 96.44%	99.83% 99.87%
WF-4	75.91% 91.19%	76.64% 91.32%	93.97% 96.69%

TABLE 7: Array-3 probability of AoA estimation using 1025 snapshots ($0 \text{ dB} \leq \text{SNR} \leq 10 \text{ dB}$).

	Both Az and El, $ \text{Er} \leq 1^\circ$ $ \text{Er} \leq 5^\circ$	Az, $ \text{Er} \leq 1^\circ$ $ \text{Er} \leq 5^\circ$	El, $ \text{Er} \leq 1^\circ$ $ \text{Er} \leq 5^\circ$
WF-1	83.86% 96.19%	83.99% 96.27%	99.69% 99.78%
WF-2	83.11% 95.82%	83.22% 95.92%	99.71% 99.77%
WF-3	84.75% 96.14%	83.81% 96.20%	99.77% 99.85%
WF-4	59.92% 80.77%	61.85% 81.10%	82.06% 90.45%

TABLE 8: Array-3 probability of AoA estimation using 1025 snapshots ($-10 \text{ dB} \leq \text{SNR} \leq 0 \text{ dB}$ and last line using 513 snapshots).

	Both Az and El, $ \text{Er} \leq 1^\circ$ $ \text{Er} \leq 5^\circ$	Az, $ \text{Er} \leq 1^\circ$ $ \text{Er} \leq 5^\circ$	El, $ \text{Er} \leq 1^\circ$ $ \text{Er} \leq 5^\circ$
WF-1	53.63% 81.48%	56.60% 81.54%	83.20% 91.35%
WF-2	52.32% 80.07%	55.31% 80.17%	82.03% 90.55%
WF-3	52.75% 80.66%	55.47% 80.72%	83.31% 90.11%
WF-4	26.30% 51.05%	30.01% 52.22%	49.32% 69.31%
WF-4	33.28% 67.64%	38.46% 67.93%	64.92% 83.51%

TABLE 9: Array-3 probability of AoA estimation using 1025 snapshots ($-20 \text{ dB} \leq \text{SNR} \leq -10 \text{ dB}$ and last line using 513 snapshots).

	Both Az and El, $ \text{Er} \leq 1^\circ$ $ \text{Er} \leq 5^\circ$	Az, $ \text{Er} \leq 1^\circ$ $ \text{Er} \leq 5^\circ$	El, $ \text{Er} \leq 1^\circ$ $ \text{Er} \leq 5^\circ$
WF-1	3.33% 21.27%	7.14% 23.51%	17.46% 45.82%
WF-2	3.18% 20.74%	7.16% 23.14%	16.65% 45.60%
WF-3	3.18% 21.51%	7.21% 23.89%	17.68% 46.09%
WF-4	1.21% 9.10%	3.20% 11.76%	9.20% 31.07%
WF-4	1.05% 10.04%	3.32% 12.73%	9.36% 33.10%

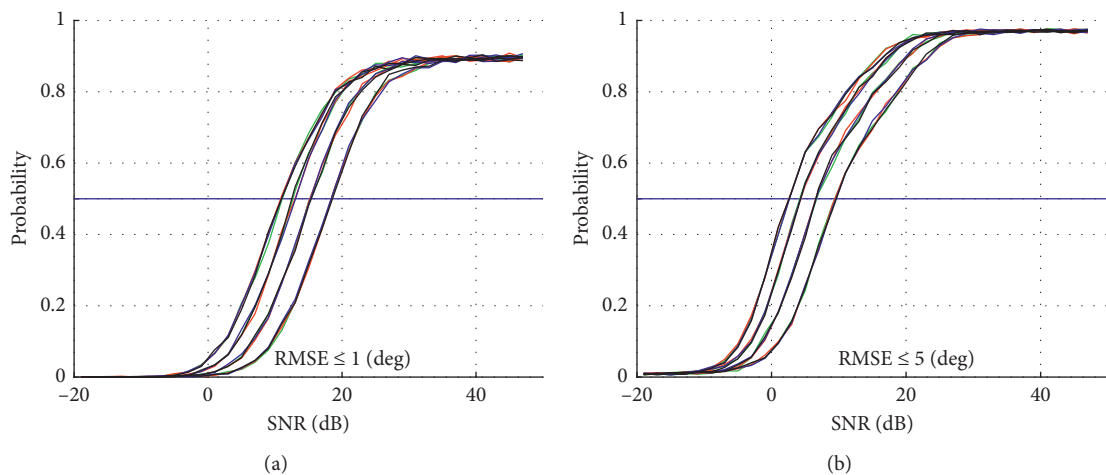
FIGURE 14: Probability of AoA estimation of Array-3 for 4 waveforms with $M + 1 = 2, 3, 5,$ and 9 , from right to left in each subplot.



FIGURE 15: Six planar arrays; black dots are the 7-element NSA (see the text for more details).

15 dB SNR and 3 snapshots, the method can have 50% probability of AoA estimation with $RMSE \leq 1^\circ$.

6.5. Discussion. From all the subplots (a) in Figures 3–5 and Figure 14, one can find that, just by increasing SNR, it cannot make the method to yield close to 100% probability of AoA estimation with $RMSE \leq 1^\circ$. This is

determined by the density of the angles on the 2D-angle grid (for example, $P_{total} = 29495$ in this study) in the 7-element NSA FOV and the number of frequency samples ($F_{total} = 2401$) in [6, 18] GHz used to precalculate SV and \mathfrak{F} databases. Increasing these numbers will enhance the performance of the method. However, it will slow down the calculation on a regular desktop computer. By using other means of hardware such as dedicated FPGA with

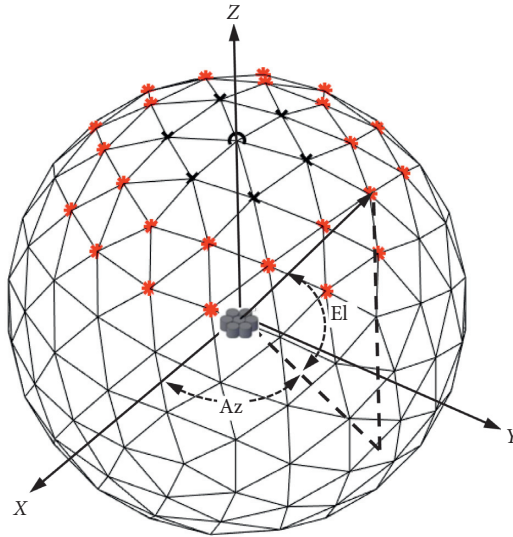


FIGURE 16: An example of a 2D-angle grid formed by an icosphere-based mesh; 7-element NSA phase-reference center and the icosphere center are collocated at the origin of the XYZ-coordinate system.

TABLE 10: Different 2D-angle grids.

N_{subdiv}	Number of angles within FOV (P_{total})	Rough order of angle resolution (deg)
4	462	4.32
5	1841	2.16
6	7371	1.08
7	29495	0.54
8	117927	0.27

The bold text indicates that $N_{\text{subdiv}} = 7$ is used in this study.

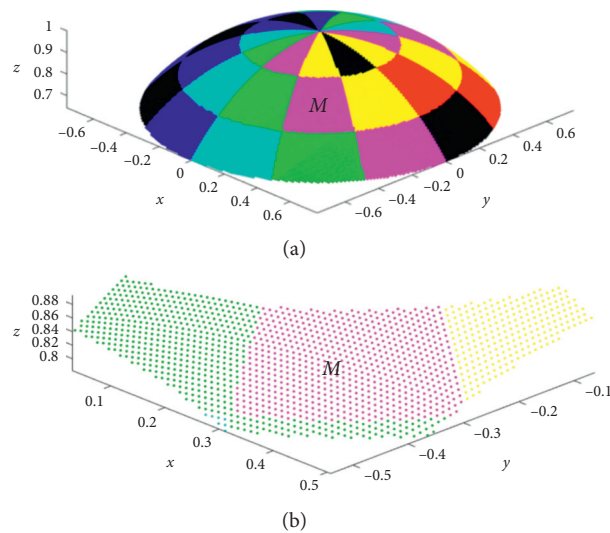


FIGURE 17: (a) The 2D-angle grid in the 7-element FOV ($N_{\text{subdiv}} = 7$). The grid is subdivided into 36 angle zones that are defined by 12 equal divisions in Az-angle and 3 divisions in El-angle, i.e., $[40^\circ \text{ to } 53^\circ]$, $[53^\circ \text{ to } 70^\circ]$, and $[70^\circ \text{ to } 90^\circ]$. (b) A zoom-in plot of zone M in (a).

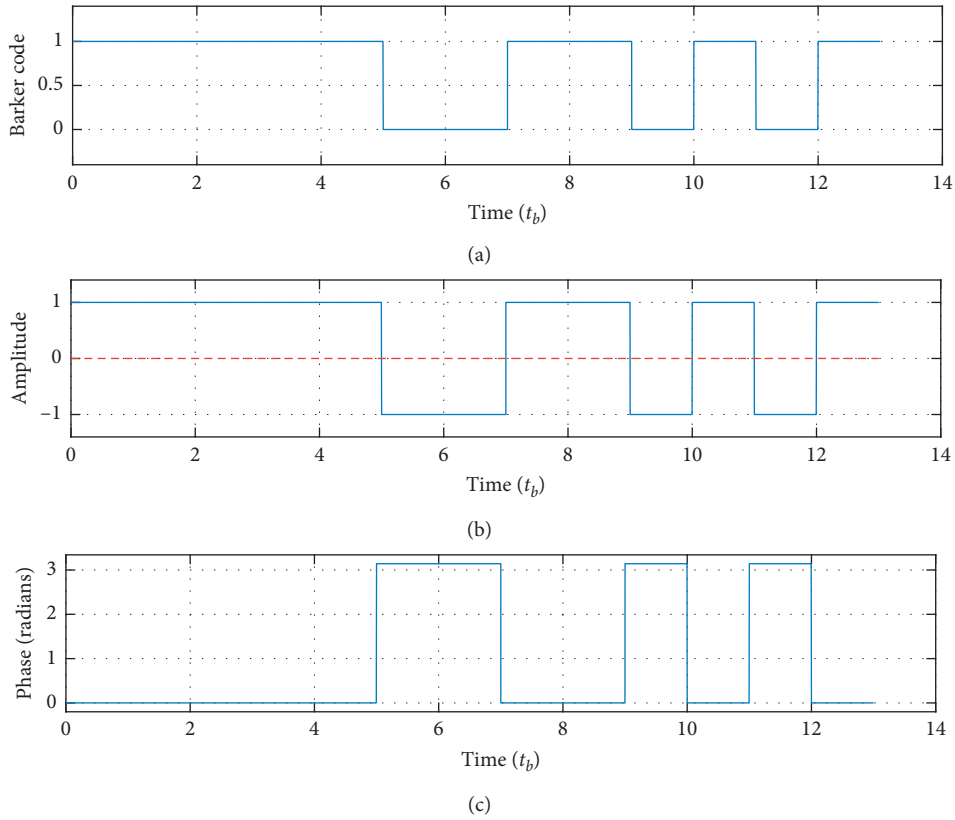


FIGURE 18: One pulse of Barker code: (a) 13-chip Barker code, (b) the Barker code I/Q waveform (solid and dashed lines are I and Q , respectively), and (c) phase in each chip of I/Q signal.

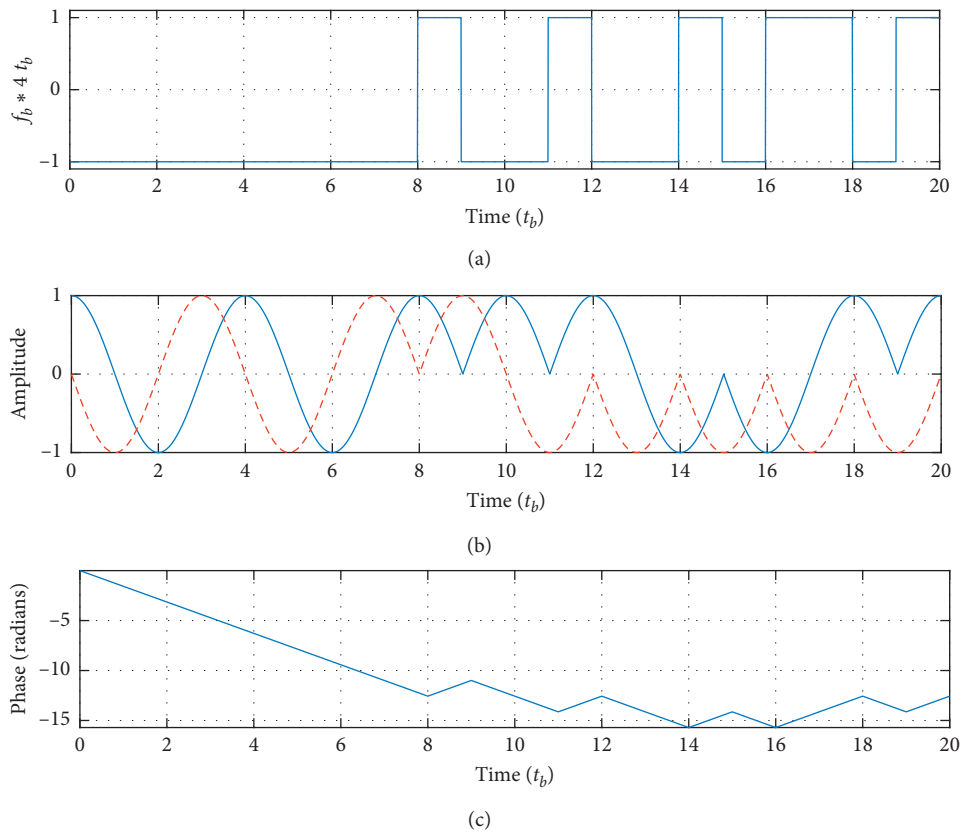


FIGURE 19: One pulse of a two-valued frequency-coded waveform: (a) a 20-chip two-valued frequency code, i.e., [00000000100100101 1 0 1], (b) the I/Q of the waveform (solid and dashed lines are I and Q , respectively), and (c) the phase in each chip of the signal.

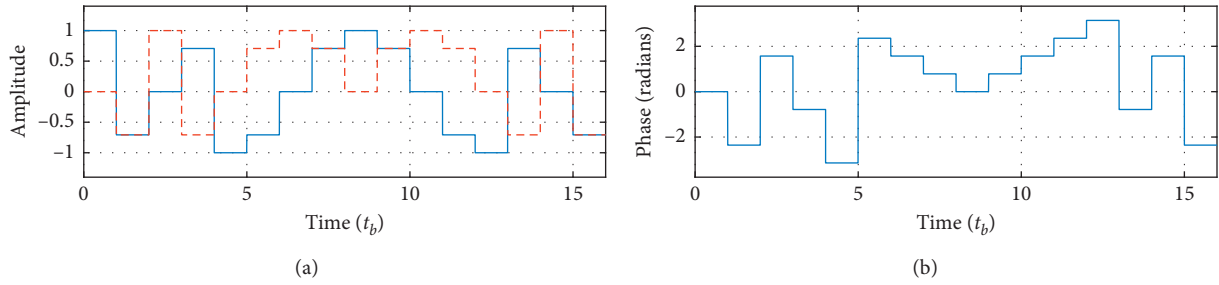


FIGURE 20: A pulse of a 16-chip P1 poly-phase waveform: (a) I/Q of the waveform (solid and dashed lines are I and Q , respectively) and (b) the phase in each chip of the signal.

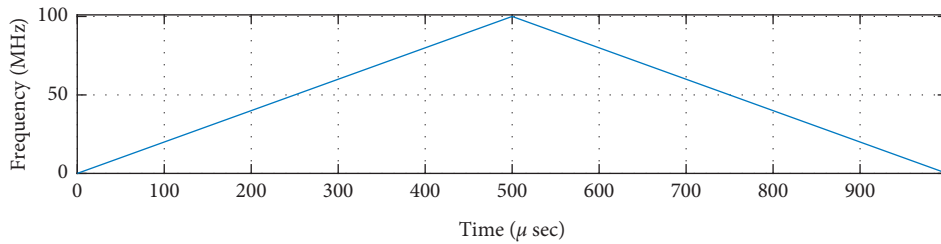


FIGURE 21: One period of a FMCW waveform.

TABLE 11: FMCW signal parameters.

Sweep bandwidth (MHz)	Sweep direction	Sweep time	Number of sweeps
100	Triangle	500 μ s	2

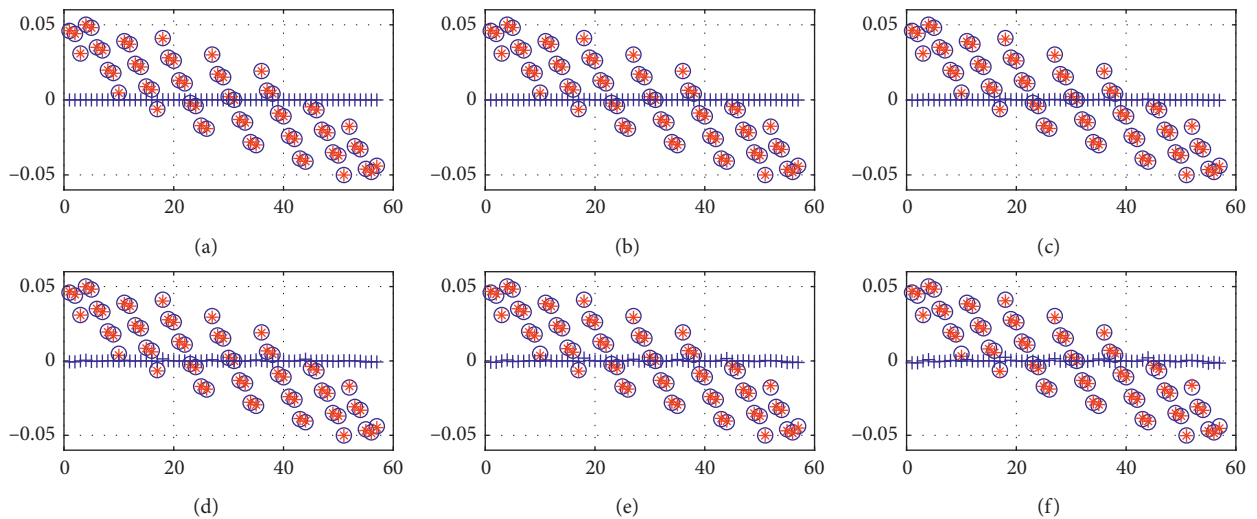


FIGURE 22: The comparison between the values of the first term (blue oooo) and the imaginary part of the second term (red ***) of (D.2) with $SNR = \infty$, when the frequency is at 10 GHz, the incident direction is from $(143.75^\circ \ 84.66^\circ)$ to Array-3, the waveform is WF-1, and the number of snapshots is 512. Blue plus signs are the real part of the second term in (D.2). (a) Freq=6 GHz; (b) Freq=8 GHz; (c) Freq=10 GHz; (d) Freq=14 GHz; (e) Freq=16 GHz; (f) Freq=18 GHz.

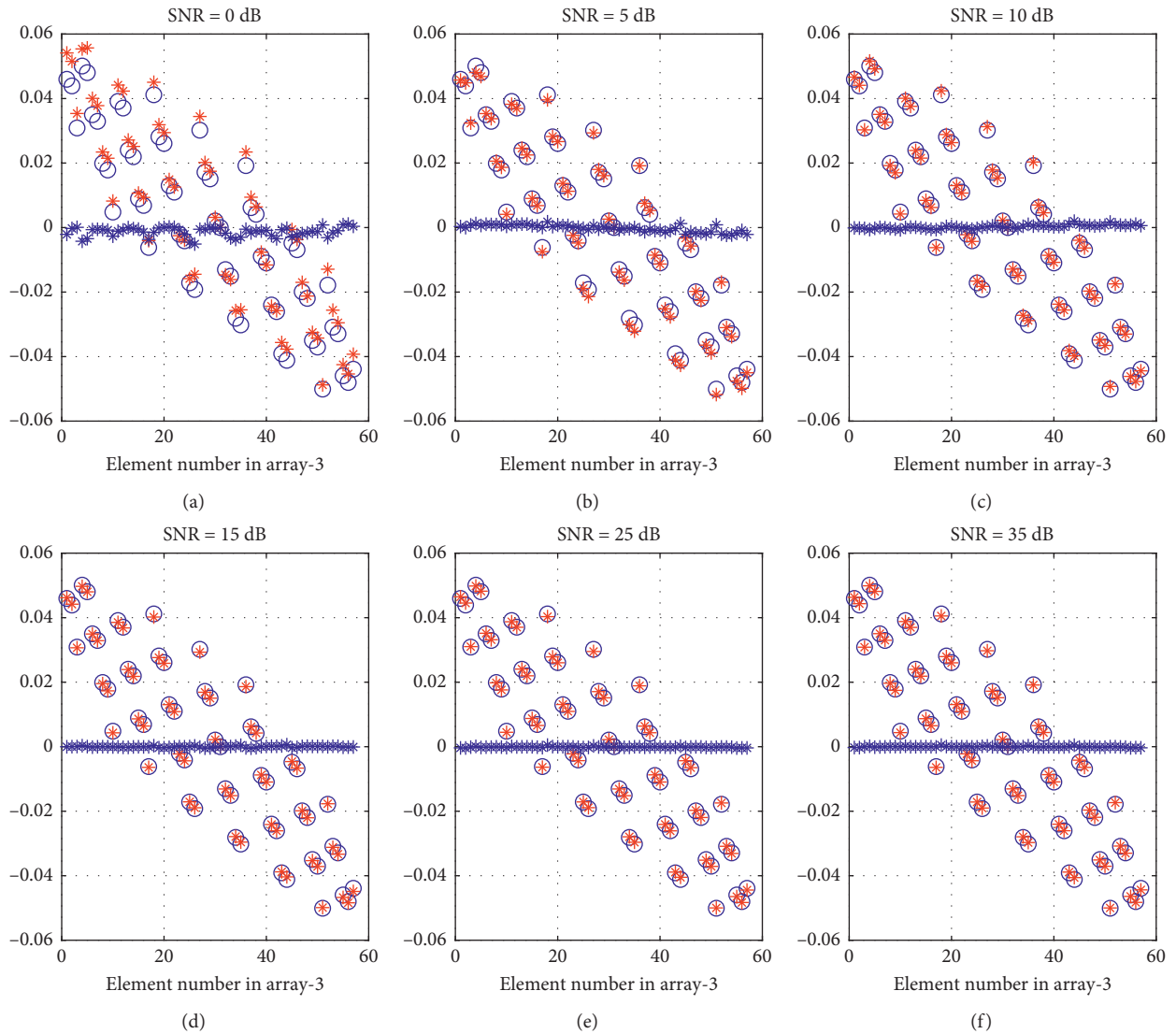


FIGURE 23: The comparison between the values of the first-term (blue oooo) and the imaginary part of the second-term (red ****) of (D.2) with different SNRs, when the frequency is at 10 GHz, the incident direction is from $(143.75^\circ \ 84.66^\circ)$ to Array-3, the waveform is WF-1 and the number of snapshots is 512. Blue plus signs are the real part of the second term in (D.2). (a) SNR = 0 dB; (b) SNR = 5 dB; (c) SNR = 10 dB; (d) SNR = 15 dB; (e) SNR = 25 dB; (f) SNR = 35 dB.

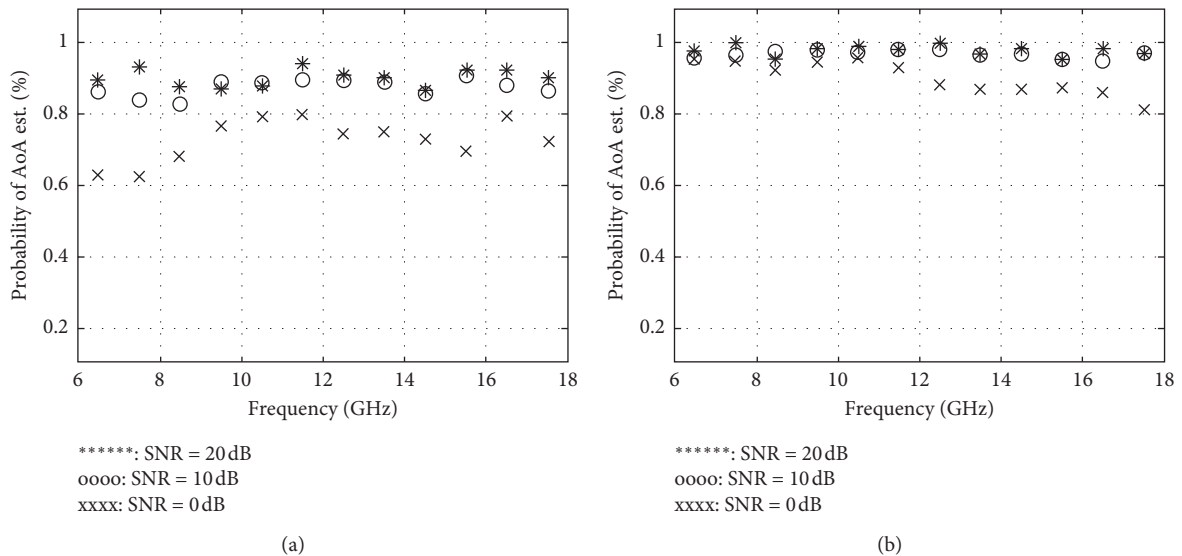


FIGURE 24: Frequency vs probability of AoA estimation for Array-3 and WF-1 with 512 snapshots: (a) $RMSE \leq 1^\circ$ and (b) $RMSE \leq 5^\circ$.

fast access memory, the speed of the calculation can be accelerated.

7. Conclusions

This paper introduces a new radar signal AoA estimator using a 7-element 6–18 GHz CBSA NSA and a 2D D3 method suitable for ESM applications. Unlike the 3- and 5-element CBSA arrays that are commonly used by interferometry-based AoA methods, our array can be installed on small airborne platforms. The paper also introduces a 2D calibration and data-transformation method that allows an IEPA to use the 7-element NSA-measured data for AoA estimations and converts a full 3D antenna problem into a 3D free-space problem. To calculate the AoA, a new 2D AoA search method has been developed by taking the advantages of the SV of the IEPA and 2D D3 results, which avoids having to resolve the ambiguity encountered in interferometer arrays and also results in frequency-independent performance. The simulation results show that with high SNR (≥ 15 dB), the estimator can have 50% probability of AoA estimation with $\text{RMSE} \leq 1^\circ$ using just few temporal samples. More importantly, with more temporal snapshots, the estimator has 52% and 80% probabilities of AoA estimation with $\text{RMSE} \leq 1^\circ$ and 5° , respectively, for phase- or frequency-modulated radar pulses, when the SNR is between -10 and 0 dB. Although the performance can degrade for an ultra-wideband FMCW radar signal (for example, the 100 MHz chirp-signal used here), it can still achieve 33% and 67% probabilities of AoA estimation with $\text{RMSE} \leq 1^\circ$ and 5° , respectively, when SNR is between -10 dB and 0 dB. Future work is needed to improve the performance of the AoA estimation for ultra-wideband FMCW signals in low SNR conditions. The study also shows that the estimator prefers a circular-shaped planar array with a triangular interelement pattern, since this array presents more symmetrical characteristics when it is seen from different Az angles. In order to facilitate the practical use of this AoA estimator in ESM applications, i.e., as there is no a priori knowledge of the SOI, this paper also presents the use of precalculated SV and \mathfrak{S} -databases, which are built on a 2D-angle-grid with more uniformly distributed directions with a set of preselected frequency points. The AoA calculation can be further improved by using a denser 2D-angle-grid, more frequency points for database calculations, and dedicated hardware with fast access memory.

Appendix

A. 2D Planar Arrays with Isotropic Elements

Six different shapes of planar arrays were used in the study. These arrays are shown from Figure 15, and they are as follows:

- (i) Array-1 (a): uniform-spaced rectangular array with 81 elements (white circles); element spacing is 7 mm in both x and y directions. The array center is at the 41st element.
- (ii) Array-2 (b): uniform-spaced hexagonal array with 61 elements (white circles); the element spacing in

each triangular is 7 mm in both x and y directions. The array center is at the 31st element.

- (iii) Array-3 (c): circular planar array with triangular grid with 57 elements (white circles); the element spacing in each triangular grid is 7 mm. The array center is at the 31st element.
- (iv) Array-4 (d): hexagonal planar array with rectangular grid with 77 elements (white circles); the element spacing is 7 mm in both x and y directions. The array center is at the 39th element.
- (v) Array-5 (e): circular planar array with rectangular grid with 69 elements (white circles); the element spacing is 7 mm in both x and y directions. The array center is at the 35th element.
- (vi) Array-6 (f): rectangular planar array with triangular grid with 81 elements (white circles); the element spacing in each triangular grid is 7 mm. The array center is at the 41st element.

The following can be found:

- (i) Arrays have different isotropic-element distribution patterns;
- (ii) Since the patterns are different, the total number of isotropic elements (NN) is also different;
- (iii) The aperture size of each plane array is about the same as that of the 7-element NSA;
- (iv) The center element in an array is collocated with the first element of the 7-element NSA.

B. Definition of 2D-Angle Grid by Vertices of a Unit Icosphere

It is known that the incident angles defined on a UV-sphere [62], which are frequently used in antenna analysis, have much more dense directions near north and south poles than near the equator. In order to obtain more uniform angular distributions for AoA searching using (18), a 2D-angle grid defined by the unit icosphere [63] is used in this study. The 2D-angle grid is formed by subdividing the triangles of a regular icosahedron, and the number of subdivisions (N_{subdiv}) determines the density of the vertices on the surface of an icosphere [64]. Figure 16 shows an example of the 2D-angle grid. Since the CBSA has about 100° 3 dB antenna beamwidth, in this study, the FOV of the 7-element NSA is defined within $[Az_1 Az_2] \times [El_1 El_2] = [-180^\circ 180^\circ] \times [40^\circ 90^\circ]$, which are indicated by the asterisks in the example shown in Figure 16.

Table 10 gives the number of total directions (vertices) within the FOV and their corresponding angular resolutions with respect to the number of subdivisions of the triangles of a regular icosahedron. Averaged El-angle difference between the vertex on z -axis and surrounding 6 vertices (marked by “x” in Figure 16) gives a rough order of angle resolution. Considering the AoA estimation accuracy and calculation speed, $N_{\text{subdiv}} = 7$ is used in this study. This 2D-angle grid with angle zones within the FOV is shown in Figure 17.

C. Four Commonly Used Radar Signals

C.1. Barker Code of Length Equal to 13. The 13-chip Barker code is shown in Figure 18, which is a binary-phase shift-keying modulation. In our simulations, the duration of each chip (t_b) is 200 ns, so the total pulse width (PW) is 2.6 μ s.

C.2. Two-Valued Frequency-Coded Waveform. Figure 19 shows the information of a 20-chip two-valued frequency-coded waveform, which is given in Table I of [58]. The two-valued frequency-coded waveforms presented in [58] can yield near-perfect periodic autocorrelation function for radar applications, when the number of chips is a multiple of 4 and the frequency values are $\pm 1/4t_b$, where t_b is the bit duration. The duration of each chip in Figure 19 is 200 ns, and the total PW is 4 μ s. The two frequency values are ± 1.25 MHz. This 20-chip two-valued frequency-coded waveform is a kind of binary-frequency shift-keying modulation.

C.3. Poly-Phase Waveform. A 16-chip P1 poly-phase waveform is shown in Figure 20. Each chip width is 1 μ s, and the total PW is 16 μ s.

C.4. FMCW. The frequency change of the FMCW waveform used in this study is shown in Figure 21. Its parameters are given in Table 11. Note that it has a very wide linear frequency change during chirping.

D. Explanation of the Frequency-Independent Performance

From Figures 6–8, one can observe that, for a given AoA estimation accuracy requirement (e.g., $\text{RMSE} \leq 1^\circ$) and the probability of AoA estimation (e.g., 50%), the required SNR is close to a constant, when the frequency is from 6 to 18 GHz. The following gives the explanation.

Taking natural log of both (15) and squared of (17), (18) can be rewritten as

$$\min_{\substack{az=az_e \\ el=el_e}} \left\{ \left(\frac{1}{\lambda_{\text{est}}} \right) \sum_{n=1}^{NN} j4\pi [px_n \cos(el)\cos(az) + py_n \cos(el)\sin(az)] - \lambda_{\text{est}} \ln \left[\frac{1}{C} \sum_{m=1}^M x_n^2(m)w_m \right] \right\}. \quad (\text{D.1})$$

In this equation, the $\lambda_{\text{est}}^{-1}$ term can be removed, as it is a constant. Then, one has the following equation:

$$\min_{\substack{az=az_e \\ el=el_e}} \left\{ \sum_{n=1}^{NN} j4\pi [px_n \cos(el)\cos(az) + py_n \cos(el)\sin(az)] - \lambda_{\text{est}} \ln \left[\frac{1}{C} \sum_{m=1}^M x_n^2(m)w_m \right] \right\}. \quad (\text{D.2})$$

It can be seen that during the solution search, the second term (after the minus sign in (D.2)) has to match or be very close to a variable (the first term before minus sign in (D.2)), which is only determined by the direction and locations of the elements in an IEPA. Since the first term is frequency independent, the second term must also be frequency independent. The following simulation results support this conclusion.

Figure 22 shows the comparison between the first term and the imaginary part of the second term in (D.2) at each element in Array-3, when SNR is equal to infinity. One can see that the imaginary part of the second term in (D.2) does not change when the frequency changes at a given incident direction.

Figure 23 shows that the values of the first term and the imaginary part of the second term in (D.2) at each element in Array-3 get closer to each other as SNR improves. The performances of the probability of AoA estimation at different frequencies are close to each other at different SNR levels as shown in Figure 24.

Data Availability

The ways to generate the simulation data used to support the findings of this study are included within the article.

Conflicts of Interest

The authors declare that there are no conflicts of interest regarding the publication of this paper.

Acknowledgments

This research was supported by the Radar Electronic Warfare Capability Development in Radar Electronic Warfare Section at Defence Research and Development Canada-Ottawa Research Centre, Department of National Defence, Canada. Special thanks to Mr. Michael Low from Defence Research and Development Canada for many good discussion and comments to improve the quality of the paper.

References

- [1] P. E. Pace, *Detecting and Classifying Low Probability of Intercept Radar*, Artech House, Norwood, MA, USA, 2nd edition, 2009.
- [2] E. Jacobs and E. Ralston, "Ambiguity resolution in interferometry," *IEEE Transactions on Aerospace and Electronic Systems*, vol. AES-17, no. 6, pp. 766–780, 1981.
- [3] W. B. Kendall, "Unambiguous accuracy of an interferometer angle-measuring system," *IEEE Transactions on Space Electronics and Telemetry*, vol. SET-11, no. 2, pp. 62–70, 1965.
- [4] R. C. Hansen, "Microwave scanning antennas," in *Array Systems*, vol. 3, Academic Press, Cambridge, MA, USA, 1966.
- [5] K. Pasala, R. Penno, and S. Schneider, "Novel wideband Multimode hybrid interferometer system," *IEEE Transactions on Aerospace and Electronic Systems*, vol. 39, no. 4, pp. 1396–1406, 2003.
- [6] E. Stephen Lipsky, *Microwave Passive Direction Finding*, Scitech Publishing, Inc., Raleigh, NC, USA, 2004.
- [7] J. B. Y. Tsui, *Microwave Receivers with Electronic Warfare Applications*, John Wiley & Sons, Hoboken, NJ, USA, 1986.
- [8] F. Neri, *Introduction to Electronic Defence Systems*, Artech House, Norwood, MA, USA, 2nd edition, 2006.
- [9] S. Chandran, *Advances in Direction-of-Arrival Estimation*, Artech House, Norwood, MA, USA, 2006.
- [10] A. De Martino, *Introduction to Modern EW Systems*, Artech House, Norwood, MA, USA, 2012.
- [11] T. E. Tuncer and B. Friedlander, *Classical and Modern Direction-of-Arrival Estimation*, Academic Press, Burlington, MA, USA, 2009.
- [12] R. Schmidt, "Multiple emitter location and signal parameter estimation," *IEEE Transactions on Antennas and Propagation*, vol. 34, no. 3, pp. 276–280, 1986.
- [13] R. Roy and T. Kailath, "ESPRIT-estimation of signal parameters via rotational invariance techniques," *IEEE Transactions on Acoustics, Speech, and Signal Processing*, vol. 37, no. 7, pp. 984–995, 1989.
- [14] X. Wang, L. Wan, M. Huang, C. Shen, and K. Zhang, "Polarization channel estimation for circular and non-circular signals in massive MIMO systems," *IEEE Journal of Selected Topics in Signal Processing*, vol. 13, no. 5, pp. 1001–1016, 2019.
- [15] H. Chen, C. Hou, W.-P. Zhu et al., "ESPRIT-like two-dimensional direction finding for mixed circular and strictly noncircular sources based on joint diagonalization," *Signal Processing*, vol. 141, pp. 48–56, 2017.
- [16] M. Coutino, R. Pribic, and G. Leus, "Direction of arrival estimation based on information geometry," in *Proceedings of the 2016 IEEE International Conference on Acoustics, Speech and Signal Processing (ICASSP)*, pp. 3066–3070, Shanghai, China, March 2016.
- [17] Y.-Y. Dong, C.-X. Dong, W. Liu, M.-M. Liu, and Z.-Z. Tang, "Scaling transform based information geometry method for DOA estimation," *IEEE Transactions on Aerospace and Electronic Systems*, vol. 55, no. 6, pp. 3640–3650, 2019.
- [18] A. D. Lonkeng and J. Zhuang, "Two-dimensional DOA estimation using arbitrary arrays for massive MIMO systems," *International Journal of Antennas and Propagation*, vol. 2017, Article ID 6794920, 9 pages, 2017.
- [19] V. Krishnaveni, T. Kesavamurthy, and B. Apama, "Beamforming for direction of arrival (DOA) estimation—a survey," *International Journal of Computer Applications*, vol. 61, no. 11, 2013.
- [20] M. Devendra and K. Manjunathachari, "Literature survey on high resolution direction of arrival (DOA) algorithms," *International Advanced Reserch Journal in Science, Engineering and Technology*, vol. 2, no. 2, pp. 23–31, 2015.
- [21] S. Barua, S. C. Lam, P. Ghosa, S. Xing, and K. Sandrasegaran, "A survey of direction of arrival estimation techniques and implementation of channel estimation based on SCME," in *Proceedings of the 2015 12th International Conference on Electrical Engineering/Electronics, Computer, Telecommunications and Information Technology (ECTI-CON)*, pp. 1426–1429, Hua Hin, Thailand, June 2015.
- [22] Z. Zheng and S. Mu, "Two-dimensional DOA estimation using two parallel nested arrays," *IEEE Communications Letters*, vol. 24, no. 3, pp. 568–571, 2020.
- [23] H. P. Shi, W. Leng, Z. W. Guan, and T. Z. Jin, "Two novel two-stage direction of arrival estimation algorithms for two-dimensional mixed noncircular and circular sources," *Sensors*, vol. 17, no. 6, p. 1433, 2017.
- [24] Y. Wu, G. S. Liao, and H. C. So, "A fast algorithm for 2-D directional-of-arrival estimation," *Signal Processing*, vol. 83, no. 8, pp. 1927–1831, 2003.
- [25] A.-J. van der Veen, "Asymptotic properties of the algebraic constant modulus algorithm," *IEEE Transactions on Signal Processing*, vol. 49, no. 8, pp. 1796–1807, 2001.
- [26] Q. Wang, H. Yang, H. Chen, Y. Y. Dong, and L. H. Wang, "A low complexity method for two-dimensional direction-of-arrival estimation using an L-shaped array," *Sensors (Basel, Switzerland)*, vol. 17, no. 12, p. 190, 2017.
- [27] A. B. Gershman, M. Rübsamen, and M. Pesavento, "One- and two-dimensional direction-of-arrival estimation: an overview of search-free techniques," *Signal Processing*, vol. 90, no. 5, pp. 1338–1349, 2010.
- [28] S. O. Al-Jazzar, Z. Hamici, and S. Aldalahmeh, "Two-dimensional AoA estimation based on a constant modulus algorithm," *International Journal of Antennas and Propagation*, vol. 2017, Article ID 3214021, 6 pages, 2017.
- [29] E. J. Candes and T. Tao, "Decoding by linear programming," *IEEE Transactions on Information Theory*, vol. 51, no. 12, pp. 4203–4215, 2005.
- [30] D. L. Donoho, "Compressed sensing," *IEEE Transactions on Information Theory*, vol. 52, no. 4, pp. 1289–1306, 2006.
- [31] E. J. Candes, J. Romberg, and T. Tao, "Robust uncertainty principles: exact signal reconstruction from highly incomplete frequency information," *IEEE Transactions on Information Theory*, vol. 52, no. 2, pp. 489–509, 2006.
- [32] A. C. Gurbuz, J. H. McClellan, and V. Cevher, "A compressive beamforming method," in *Proceedings of the International Conference on Acoustics, Speech, and Signal Processing*, Las Vegas, NV, USA, March 2008.
- [33] A. C. Gurbuz, V. Cevher, and J. H. McClellan, "Bearing estimation via spatial sparsity using compressive sensing," *IEEE Transactions on Aerospace and Electronic Systems*, vol. 48, no. 2, pp. 1358–1369, 2012.
- [34] V. Cevher, A. C. Gurbuz, J. H. McClellan, and R. Chellappa, "Compressive wireless arrays for bearing estimation," in *Proceedings of the 2008 IEEE International Conference on Acoustics, Speech and Signal Processing*, pp. 2497–2500, Las Vegas, NV, USA, March 2008.
- [35] E. Candes and T. Tao, "The dantzig selector: statistical estimation when p is much larger than n," *The Annals of Statistics*, vol. 35, no. 6, pp. 2313–2351, 2007.
- [36] C. Wu and J. Elangage, "Multi-emitter 2-dimensional angle-of-arrival estimator via compressive sensing," *IEEE Transactions on Aerospace and Electronic Systems*, vol. 56, no. 4, pp. 2884–2895, 2020.

- [37] Z.-M. Liu, Z.-T. Huang, Y.-Y. Zhou, and J. Liu, "Direction-of-arrival estimation of noncircular signals via sparse representation," *IEEE Transactions on Aerospace and Electronic Systems*, vol. 48, no. 3, pp. 2690–2698, 2012.
- [38] Z.-M. Liu, Z.-T. Huang, and Y.-Y. Zhou, "Array signal processing via sparsity-inducing representation of the array covariance matrix," *IEEE Transactions on Aerospace and Electronic Systems*, vol. 49, no. 3, pp. 1710–1724, 2013.
- [39] Z. Yang, J. Li, P. Stoica, and L. Xie, "Sparse methods for direction-of-arrival estimation," *Academic Press Library in Signal Processing*, Elsevier, vol. 7, pp. 509–581, Oxford, UK, 2018.
- [40] J. Cai, W. Liu, R. Zong, and B. Wu, "Sparse array extension for non-circular signals with subspace and compressive sensing based DOA estimation methods," *Signal Processing*, vol. 145, pp. 59–67, 2018.
- [41] Z. Zhang and B. D. Rao, "Sparse signal recovery with temporally correlated source vectors using sparse Bayesian learning," *IEEE Journal of Selected Topics in Signal Processing*, vol. 5, no. 5, pp. 912–926, 2011.
- [42] M. Carlin, P. Rocca, G. Oliveri, and A. Massa, "Bayesian compressive sensing as applied to directions-of-arrival estimation in planar arrays," *Journal of Electrical and Computer Engineering*, vol. 2013, Article ID 245867, 12 pages, 2013.
- [43] P. Rocca, M. A. Hannan, M. Salucci, and A. Massa, "Single-snapshot DoA estimation in array antennas with mutual coupling through a multiscaling BCS strategy," *IEEE Transactions on Antennas and Propagation*, vol. 65, no. 6, pp. 3203–3213, 2017.
- [44] T. K. Sarkar, S. Nagaraja, and M. C. Wicks, "A deterministic direct data domain approach to signal estimation utilizing nonuniform and uniform 2-D arrays," *Digital Signal Processing*, vol. 8, no. 2, pp. 114–125, 1998.
- [45] T. K. Sarkar, T. K. Sarkar, H. Wang et al., "A deterministic least-squares approach to space-time adaptive processing (STAP)," *IEEE Transactions on Antennas and Propagation*, vol. 49, no. 1, pp. 91–103, 2001.
- [46] K. Kim, T. K. Sarkar, and M. S. Palma, "Adaptive processing using a single snapshot for a non-uniformly spaced array in the presence of mutual coupling and near-field scatterers," *IEEE Transactions on Antennas and Propagation*, vol. 50, no. 5, pp. 582–590, 2002.
- [47] T. K. Sarkar, H. Schwarzlander, S. Seungwon Choi, M. S. Palma, and M. C. Wicks, "Stochastic versus deterministic models in the analysis of communication systems," *IEEE Antennas and Propagation Magazine*, vol. 44, no. 4, pp. 40–50, 2002.
- [48] T. K. Sarkar, M. C. Wicks, M. Salazar-Palma, and R. J. Bonneau, *Smart Antennas*, IEEE Press, A John Wiley & Son, Inc., Publication, Hoboken, NJ, USA, 2003.
- [49] K. J. Kim, T. K. Sarkar, H. Wang, and M. Salazar-Palma, "Direction of arrival estimation based on temporal and spatial processing using a direct data domain (D3) approach," *IEEE Transactions on Antennas and Propagation*, vol. 52, no. 2, pp. 533–541, 2004.
- [50] H. Chen, B. X. Huang, Y. L. Wang, and Y. Q. Hou, "Direction-of-arrival based on direct data domain (D3) method," *Journal of Systems Engineering and Electronics*, vol. 20, no. 3, pp. 512–518, 2009.
- [51] W. Mao, G. Li, X. Xie, and Q. Yu, "DOA estimation of coherent signals based on direct data domain under unknown mutual coupling," *IEEE Antennas and Wireless Propagation Letters*, vol. 13, pp. 1525–1528, 2014.
- [52] P. Zhang, J. Li, A. Z. Zhou, H. B. Xu, and J. Bi, "A robust direct data domain least squares beamforming with sparse constraint," *Progress In Electromagnetics Research C*, vol. 43, pp. 53–65, 2013.
- [53] N. Yilmazer and T. K. Sarker, "2D unitary matrix pencil method for efficient direction of arrival estimation," *Digital Signal Processing*, vol. 16, pp. 767–781, 2006.
- [54] N. Yilmazer, R. Fernandez-Recio, and T. K. Sarker, "Matrix pencil method for simultaneously estimating azimuth and elevation angles of arrival along with the frequency of the incoming signals," *Digital Signal Processing*, vol. 16, pp. 796–816, 2006.
- [55] C. Wu, "Wideband miniaturized digital receiver technology for micro/nanosat application," *Scientific Report*, 2015.
- [56] E. Poliakov and C. Wu, "Compact PCI computer control system and its control software update for UAV electronic support payload," *Technical Memorandum*, 2009.
- [57] C. Wu and A. Young, "Initial design considerations of small UAV EW payload," *Technical Memorandum*, 2012.
- [58] N. Levanon and U. Levanon, "Tow-valued frequency-coded waveform with favorable periodic autocorrelation," *IEEE Transactions on Aerospace and Electronic Systems*, vol. 42, no. 1, pp. pp237–248, 2006.
- [59] X. Li and M. C. E. Yagoub, "Wideband cavity-backed spiral antenna design and mutual coupling study in a closely-spaced array," in *Proceedings of the 2018 18th International Symposium on Antenna Technology and Applied Electromagnetics (ANTEM)*, Waterloo, Canada, August 2018.
- [60] L3HARRISR Antenna System, Spiral Antenna, 2020, https://www.l3t.com/randtron/antenna_products/elements_broadband_spirals.htm.
- [61] W. A. Gardner, *Cyclostationarity in Communications and Signal Processing*, IEEE Press, Piscataway, NJ, USA, 1994.
- [62] D. Lugg, "What is the difference between a UV sphere and an icosphere?" 2020, <https://blender.stackexchange.com/questions/72/what-is-the-difference-between-a-uv-sphere-and-an-icosphere#:~:text=A%20UV%20sphere%20has%20faces,compared%20to%20the%20UV%20sphere>.
- [63] Wikipedia the Free Encyclopedia, Icosphere, 2020, <https://en.wikipedia.org/wiki/Icosphere>.
- [64] W. O. C. Ward, "Icosphere, generate unit geodesic sphere created by subdividing a regular icosahedron," 2020, <https://www.mathworks.com/matlabcentral/fileexchange/50105-icosphere?focused=3865223&tab=function>.